CODEN:LUTEDX/(TEIE-5453/1-74/(2021)

Industrial Electrical Engineering and Automation

# Evaluation of a Switched Reluctance Machine in an Automotive Oil Pump Application



**August Wahlberg**
**Edvin Malm**

Division of Industrial Electrical Engineering and Automation
Faculty of Engineering, Lund University

# Evaluation of a Switched Reluctance Machine in an Automotive Oil Pump Application

**August Wahlberg**
**Edvin Malm**

A thesis presented for the degree of
Master of Science in Mechanical Engineering

Industrial Electrical Engineering and Automation
Lund University
Sweden


LUND
UNIVERSITY

# Abstract

A Switched Reluctance Machine (SRM) is evaluated in terms of torque quality and speed ripple for a particular pump application. The aim is to give BorgWarner insight into the control methodology and possible applications for a Switched Reluctance Machine. The SRM is also compared to their current BLDC machine, used as an oil pump in their torque transfer applications. The evaluation and implementation of control methodologies is done on a 4/2 asymmetric Switched Reluctance Machine. The SRM control is developed using two different approaches, namely FEA and experimental measurement of machine characteristics. The two approaches are evaluated in regard to how well they represent the physical machine. The machine models from the FEA and the measurement differ only slightly and it is concluded that FEA is an adequate tool for developing control methods for the SRM. Two control methods, "Instantaneous Torque Control (ITC)" and "Average Torque Control (ATC)", are implemented and evaluated in regard to match the BLDC application of a speed controlled oil pump. The different control methods, ITC and ATC, are compared in regard to torque-speed performance, speed ripple and feasibility of implementation. Experimental testing is performed to validate the results. The ATC, surprisingly, has less speed ripple than the ITC which is explained by non-optimized turn off angles for the ITC. Sensorless position control is evaluated in simulation and shows that sensorless control is feasible for the SRM. The BLDC machine and the SRM are compared with respect to performance and costs. It is concluded that the BLDC is more appropriate for BorgWarner's application than the 4/2 SRM. Further studies should be conducted to examine SRMs with higher pole number configurations.

# Sammanfattning

En Switchad Reluktansmaskin (SR-maskin/SRM) utvärderas utifrån momentkvalité och hastighetsvariationer. Målet är att ge BorgWarner insikt i kontrollmetodiken samt möjliga användningsområden för en SRM. SR-maskinen jämförs med den nuvarande BLDC-maskinen som används som en oljepump i deras momentöverföringsprodukter. Utvärderingen och implementationen av kontrollmetodiken utförs på en asymmetrisk 4/2 SRM. SR-maskinens styrning utvecklas med två tillvägagångssätt, FEA och experimentell mätning av maskinens karaktäristik. De två tillvägagångssätten utvärderas utifrån hur väl de representerar den fysiska maskinen. Maskinmodellerna från FEA och mätning är i stort sett lika och det fastslås att FEA är ett användbart verktyg för utveckling av styrningen till SR-maskinen. Två styrmetoder, "Instantaneous Torque Control (ITC)" och "Average Torque Control (ATC)", implementeras och utvärderas utifrån hur väl de jämför sig med den existerande hastighetsreglerade BLDC-maskinen. De två styrmetoderna jämförs utifrån moment-hastighetsprestanda, hastighetsvariation och implementationssvårighet. Experimentell testning utförs för att validera resultaten. Förvånandsvärt nog har ATC mindre hastighetsvariation än ITC vilket förklaras med att "turn off"-vinkeln inte optimerats. Sensorlös styrning utvärderas i simulering och visar att sensorlös styrning är möjlig för SR-maskinen. BLDC-maskinen och SR-maskinen jämförs utifrån deras prestanda och kostnad. Det fastslås att BLDC-maskinen är bättre lämpad för BorgWarners användningsområde än 4/2 SR-maskinen. I framtiden bör SR-maskiner med högre poltal evalueras.

# Acknowledgements

We would like to extend our deepest gratitude to the faculty's supervisor of this project; Mats Alaküla. Without his constructive criticism and guidance, this thesis wouldn't have been possible. A special thanks to Avo Reinap who was instrumental in the FEA part of the project. We'd also like to give many thanks to the examiner of this thesis, Francisco Márquez.

The completion of this thesis wouldn't have been possible without our supervisors at BorgWarner, Markus Björk and Robin Levenhammar. They have gone out of their way in their unwavering support of this thesis. We wish to thank Johan Blomberg for pitching the idea for this thesis and for making sure that everything could proceed smoothly. The support at BorgWarner has been overwhelming with free use of their lab, testing equipment and testing rig. Beyond that we have gotten great assistance from many persons at the company; Axel Wallgren, Axel Knutsson, Simon Hed, Per Söderberg and Pierre Pettersson to mention a few. We'd like to extend our sincere thanks to all of them.

We also had the pleasure of working together with our fellow master thesis writers; Johan Appelros and Jacob Wallersköld. This thesis would not have been as fun to write without their company.

Lastly, we'd like to thank BorgWarner, as a whole, for giving us this chance and for providing us with an excellent thesis writing experience.

# Contents

# List of Figures

# List of Tables

# Nomenclature

| | |
|---|---|
| $\epsilon$ | Back EMF |
| $\lambda$ | Flux Linkage |
| $\omega$ | Angular Speed in rad/s |
| $\psi$ | Flux |
| $\theta$ | Electrical rotor position - In electrical degrees by default |
| $\theta_{el}$ | Electrical rotor position in degrees |
| $\theta_{mech}$ | Mechanical rotor position |
| $\theta_{off}$ | The electrical rotor position where a phase's commutation period ends |
| $\theta_{on}$ | The electrical rotor position where a phase's commutation period starts |
| $\zeta$ | Damping Coefficient |
| $A_c$ | Cross-sectional area of windings |
| $b$ | Frictional Coefficient |
| $I$ | Current |
| $i_{ph}$ | Phase current |
| $J$ | Mechanical Inertia |
| $L$ | Inductance |
| $l_c$ | Length of windings |
| $R$ | Resistance |
| $R_0$ | Initial resistance guess in sensorless operation |
| $R_{ph}$ | Phase resistance |
| $V$ | Voltage |
| $v_{ph}$ | Phase Voltage |

**Commutation Period** - The electric position interval in which a phase is activated

# List of acronyms

**ATC** - Average torque control
**AWD** - All-wheel-drive
**BLDC** - Brushless DC (machine)
**CAD** - Computer aided design
**CCW** - Counter clockwise
**CW** - Clockwise
**DCM** - DC machine
**el.** - electrical
**emf** - electromotive force
**FEA** - Finite element analysis
**FOC** - Field-oriented control
**IEA** - Industrial Electrical Engineering and Automation
**IM** - Induction machine
**ITC** - Instantaneous torque control
**LUT** - Look-up table
**MAB** - MicroAutoBox
**mech.** - mechanical
**PMSM** - Permanent magnet synchronous machine
**RMS** - Root mean square
**RPM** - Revolutions per minute
**SRM** - Switched reluctance machine
**SVM** - Space vector modulation
**TSF** - Torque share function

# Chapter 1

# Introduction

## 1.1 BorgWarner

BorgWarner is an automotive company with branches all around the world. Historically, in Landskrona, the company specializes in all-wheel-drive (AWD) systems having developed the Haldex clutch. While maintaining the AWD expertise, the company nowadays also operates on a broader level with driveline and propulsion systems for hybrid, electrical and combustion vehicles.

## 1.2 Problem formulation

The goal of the thesis is to evaluate the Switched Reluctance Machine's (SRM) competitiveness in means of torque quality, cost and driver requirements. The aim is to give BorgWarner insight into the control methodology and possible applications for a Switched Reluctance Machine as well as comparing it to their current BLDC machine solution. The following goals were decided on by BorgWarner, Mats Alaküla (Supervisor from IEA) and the authors of the thesis.

- Develop two or more control methodologies for an SRM, designed in regards to match the BLDC application of a speed controlled oil pump.
- Evaluate the performance without position sensors.
- Theoretically and experimentally evaluate if the SRM meets the torque and speed characteristics requirements of the BLDC.
- Compare the BLDC machine and the SRM in regard to cost of motor and driver components.

## 1.3 Background

### 1.3.1 The Switched Reluctance Machine

The Switched Reluctance machine is a primitive machine that consists of a salient rotor, usually made of laminated iron and stator poles with laminated iron cores and copper winding. Due to the lack of permanent magnets and rotor winding its construction is simple and robust in comparison to other electrical machines such as the permanent magnet synchronous machine, the DC machine and the induction machine [1, Ch. 1, pp. 25-29].

Due to the salient structure of the rotor, the magnetic reluctance varies depending on the rotor's position. This causes the inductance of the machine to be highly nonlinear which makes it challenging to minimize torque ripple and acoustic noise by means of control [1, Ch. 1, p. 27]. This sets a higher requirement on control methodology of the Switched Reluctance machine where one must analyze the characteristics of the machine's nonlinearity and customize the control methodology for each individual SRM design.

### 1.3.2 Prospects of the SRM for BorgWarner

Since electric machines are becoming even more common, with the shift towards electric vehicles and renewable energy production, BorgWarner wants to investigate other types of electric machines than the most common variants such as PMSM, BLDC and the induction machine. Since the switched reluctance machine does not require any permanent magnets it is not affected by resource scarcity or price volatility of rare earth metals, which PMSM and BLDC machines are [2] [1, Ch. 1, pp. 21-27]. Similarly to the SRM the induction machine does not require any permanent magnets, but its design is more complicated. This leads to higher manufacturing costs in comparison. Therefore, the low cost of materials and simple design makes the SRM the cheapest alternative to produce [3].

The development of SRM drivers and machine configurations is a highly researched topic. The fundamental challenges with the SRM, such as high noise levels and torque ripple, still remain. But Switched Reluctance Machines with competitive efficiencies and torque production capabilities are currently developed [4], along with performance improving drivers [5][1, Ch. 10]. Historically, the development and design of electrical machines has gone from complicated machine structures and simple drives towards simple machine structures and complicated drives. Due to the declining price of power electronics and digital control as well as stricter environmental regulations, the SRM is an interesting candidate for future machine applications [1, Ch. 1, pp. 25-29].

## 1.4 Division of work

The two authors of this thesis worked closely together throughout the whole project. In some cases, work was divided in order to work more efficiently. Some areas that were divided were "Inversion of look-up tables", "ATC optimization", "Position estimation" and "Sensorless control" where the two former were made by Edvin Malm and the two latter by August Wahlberg.

## 1.5 Outline

In the theory section, a theoretical background is provided to the working principles of the SRM. It details how a machine model is obtained and how it is used when controlling the machine. Later, different improvements that can be implemented are discussed before comparing the difference in using a position sensor and not having one. Lastly, the most common SRM converter is described.

The "Design and implementation of controller" section presents how FEA is used to produce a machine model. It describes the used microcontroller (MicroAutoBox) and power stage (RapidPro Power Unit), how they are set up (software) and connected (hardware). Subsequently, a description of the developed Simulink models and their applications is presented. After, an optimization method used for one of the control methods implemented, is described. Then, it is discussed how the position sensor is calibrated and how the friction in the testing rig is measured. Lastly, the methods of verifying the machine model, the simulation model and the control methods are presented.

The machine model from FEA simulations and experimental verification is thereafter presented in the results. Comparisons between the different control methods are shown along with results of sensorless position estimation. The results and methodology of implementing the SRM control is discussed and evaluated. The used asymmetric 4/2 SRM is compared to BorgWarner's current BLDC machine and the prospects of using an SRM for the application is discussed.

# Chapter 2

# Theory

## 2.1 Common Configurations of Switched Reluctance Machines

The Switched Reluctance Machine consists of salient, excitable stator poles and non-excitable rotor poles. The machine produces torque on the principle of the rotor's tendency to minimize its magnetic reluctance to the excited phase. This is where the name "Reluctance Machine" comes from [6, Ch. 3]. On this basis the configuration and design of a Switched Reluctance Machine can take many forms. In principle, the most basic configuration of an SRM only requires two stator poles and 2 rotor poles, denoted a "2/2" machine. Figure 2.1 shows the 2/2 SRM as well as two other configurations.

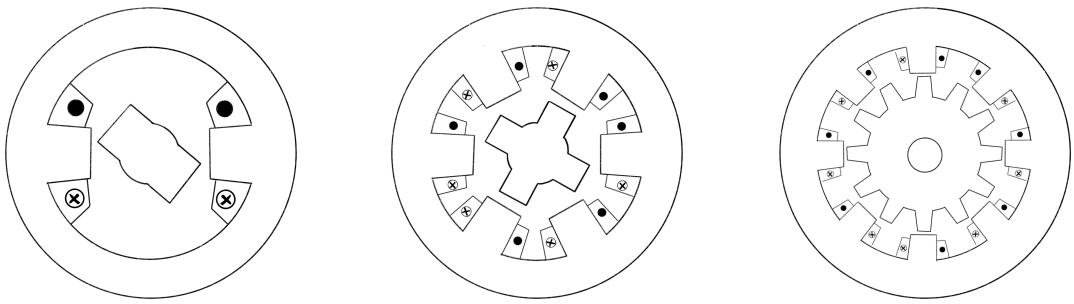

(a) 2/2 SRM (b) 6/4 SRM (c) 8/12 SRM

Figure 2.1: Three SRM configurations.

The 2/2 machine is very limited in its torque production capabilities and will be unable to produce a positive (CW) torque in half of its full rotation.

Since it is highly desirable to always be able to produce torque in an electric machine, machine configurations such as 6/4, 8/6 and 12/8 are all common. These machines all have the possibility of several phases being able to contribute to a positive torque simultaneously. Therefore, the machines can produce a smooth torque and will always be self-starting no matter the rotor's starting position. An increasing number of stator poles will lead to a reduced RMS current and is thus suitable for high power

applications. But more poles will also require a larger stator outer diameter as well as more complicated converters [1, Ch. 7, pp.254-267]. Therefore, for low cost applications, a configuration such as the 4/2 can be considered, see figure 2.2 [7]. The 4/2 machine is in itself not self-starting if the rotor is completely aligned with a stator phase. To solve this an asymmetric rotor design can be used. When one phase is active and the rotor is "locked" to it the rotor is now not completely aligned with it and the other phase can be used to start the machine. This allows self-starting at the expense of lowering the average torque production.

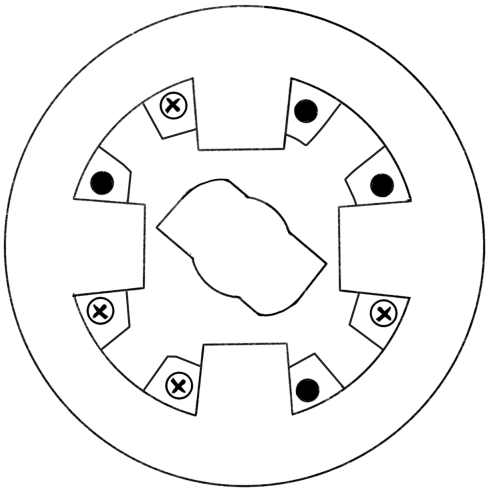

Figure 2.2: The asymmetric 4/2 Switched Reluctance Machine.

## 2.2 Working principles of the SRM

### 2.2.1 Electromagnetic Conversion

As mentioned in the previous section, an SRM works on the principle of change of reluctance in the magnetic circuit. Due to the salient structure of the rotor and stator, the reluctance will decrease as the rotor pole approaches the vicinity of the stator pole and the air gap decreases. Since the motion of the rotor changes the effective air gap, a variation in flux linkage will induce an electromotive force to limit the rate of change of current. As explained in [1, Ch. 2, pp.58-61], the majority of the magnetic energy in the magnetic circuit is stored in the high reluctance air gap. This stored air gap energy is converted into mechanical energy regarded as torque.

A magnetic circuit with high reluctance can store more energy. Since the rotor of the SRM consists of a ferromagnetic material its magnetic permeability will decrease as the material saturates. When it reaches the permeability of air it is fully saturated. It can be seen in expression 2.2 that the inductance $L(\theta)$ decreases with decreasing permeability. Looking at expression 2.3, it can be seen that this causes the magnetic energy to decrease relatively to the copper losses and the air gap energy. Relatively, a smaller part of the input energy goes to magnetic energy and more to copper losses and air gap energy (which is converted into torque). This means that a given

DC-link voltage can be better utilized if the machine runs in the saturated region. With this incentive to operate outside the linear region, a thorough machine model is needed to be able to simulate and control the SRM well [1, Ch.4 p.130].

### 2.2.2 Governing Equation of an SRM

The governing equations of a switched reluctance machine can be described by the following expression.

$$V = Ri + \frac{d\lambda}{dt} = Ri + L(\theta)\frac{di}{dt} + i\frac{dL(\theta)}{dt} = Ri + L(\theta)\frac{di}{dt} + i\frac{dL(\theta)}{d\theta}\omega \tag{2.1}$$

where $Ri$ is the voltage due to resistance in the windings, $L(\theta)\frac{di}{dt}$ is the voltage due to the inductance in the windings and $i\frac{dL(\theta)}{d\theta}\omega$ is a speed dependent voltage, analogous to the back emf (electromotive force) of a DC machine. The speed dependent voltage requires the SRM to be excited in order to produce a voltage. Therefore, in comparison to a BLDC machine the back emf cannot be measured directly by spinning the machine without exciting it. Note that equation 2.1 is only applicable when the inductance is simplified as proportional to the position and magnetic saturation is not considered. That is true only when the machine operates in its linear region. Outside of that region machine characteristics such as flux linkage and torque behave nonlinearly [1, Ch. 4].

When saturated, the relative permeability, $\mu_r$, and thus the inductance, L, decreases according to equation 2.2:

$$L = \frac{N^2}{\frac{l_c}{\mu_r \mu_0 A_c}} \tag{2.2}$$

where N is the number of winding turns, $l_c$ is the length of the winding, $A_c$ is the cross-sectional area of the winding and $\mu_0$ is the permeability of vacuum. Multiplying equation 2.1 with the current gives the expression for power, shown below in equation 2.3:

$$P = iV = Ri^2 + \frac{d}{dt}(\frac{1}{2}i^2L(\theta)) + \frac{1}{2}i^2\frac{dL(\theta)}{d\theta}\omega \tag{2.3}$$

The three terms that make up the expression can be shown to be copper heat losses, magnetic energy in the armature and the air gap energy, as seen in equation 2.4. Note that it is only the air gap energy which is transferred to mechanical energy. The copper heat losses end up heating up the machine and the surrounding air while the magnetic energy returns to the supply (in an ideal case where no energy is lost) [1, Ch.4 pp.129-130].

$$Power = copper\,heat\,losses + magnetic\,energy + air\,gap\,energy \tag{2.4}$$

## 2.3 Generating a Machine Model

In order to design adequate control methods for a Switched Reluctance Machine, one needs to know its characteristics. More specifically, one needs to know how the machine's torque and flux depend on both its rotor position and exciting stator current. Since the machine's inductance is dependent on the rotor's position relative

to the stator's external magnetic field as well as the rotor's saturation level, the machine can not be controlled in a linear fashion and its characteristics must be known beforehand in order to control it.

There are in general two different approaches used to generate such a machine model. These methods are electromagnetic finite element analysis (FEA) and direct measuring on the physical machine. They are described in sections 2.3.2 and 2.3.3.

### 2.3.1 The dynamic model/machine model

The purpose of the machine model is to represent how the physical machine behaves when voltage is applied to its phase windings. This is done with the equations and look-up tables (LUTs) seen in figure 2.3. There are two 2D-look-up tables (2 input parameters) in the dynamic model. One gives phase current as a function of electric rotor position and flux linkage (of that phase), $i_{LUT}(\theta_{el}, \lambda_{ph})$. The other one gives torque as a function of electric rotor position and phase current, $T_{LUT}(\theta_{el}, i_{ph})$. The torque, in turn, can be used to calculate the acceleration of the machine once the inertia is known. In this form, the machine model can be used in simulations to represent the physical machine. It can, however, also be used as a means to control the machine. $T_{LUT}(\theta_{el}, i_{ph})$ can be inverted to give phase current references instead, which gives it the form of $i_{LUT}(\theta_{el}, T_{ref})$. It can now be used to calculate which phase current will give a certain torque. This is very useful when controlling the machine as shown in section 2.4.1. See figure 2.4 for an example of LUTs for a symmetric machine.

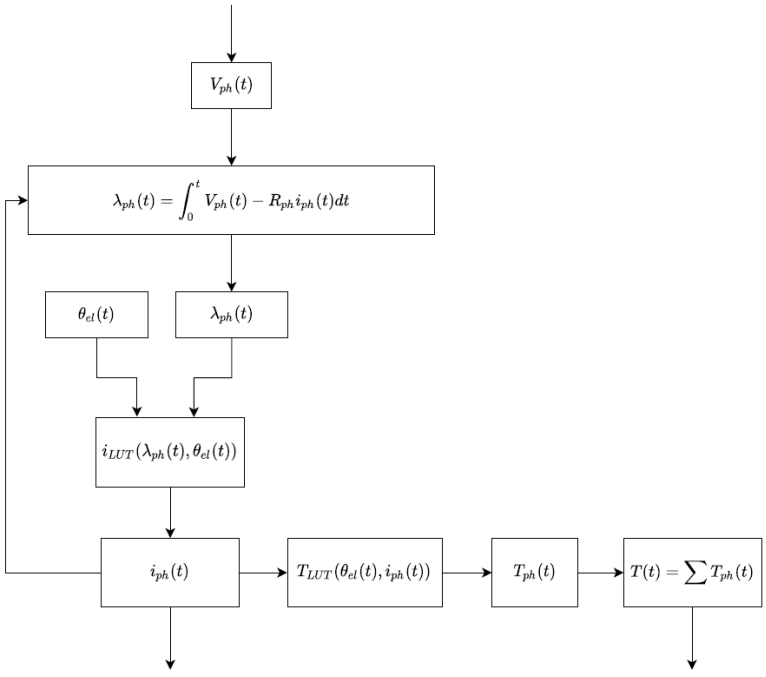


Figure 2.3: The continuous time dynamic machine model.

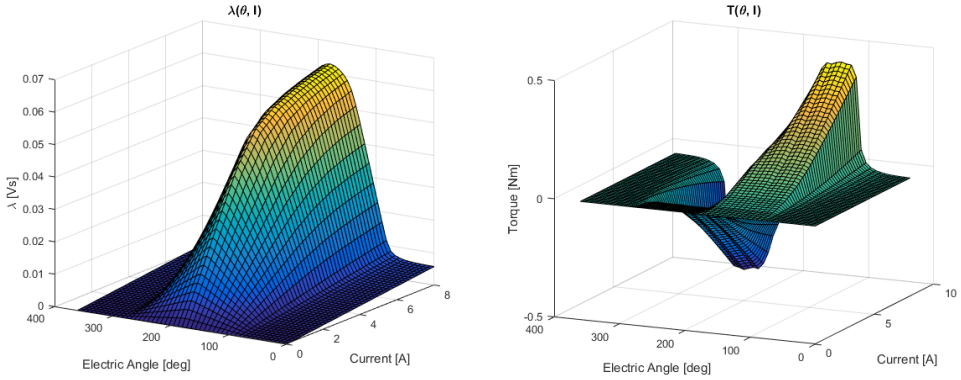


Figure 2.4: Example of Look-Up Tables (LUTs) for a symmetric Switched Reluctance Machine. Flux Linkage (left) and Torque (right) dependency on position and current is shown.

### 2.3.2 Electromagnetic Finite Element Analysis (FEA)

The mathematical objective of electromagnetic FEA is to find the electric and magnetic fields inside a boundary region. Using FEA, one can simulate the relationship between flux linkage, torque, current and rotor position relative to the excited stator position. In figure 2.5, an asymmetric 4/2 SRM can be seen in FEA with its horizontal phase excited, generating torque in the CW direction. It is outside the scope of this thesis to thoroughly explain how electromagnetic FEA works. In short, the workflow can look as follows [8].

1. Mechanical settings - Geometry is defined; e.g the rotor position, positions of phases and diameters etc. in a machine. Materials of rotor, stator, magnets, windings etc. are set.

2. Meshing - Creates a mesh (nodes connected with lines). For each mesh element, equations are set up that state how the analyzed parameter values (such as flux or magnetic fields) change from one node to another. The element density should be high in areas where the parameter values change quickly in order to solve with adequate accuracy. Triangular (2D) elements or tetrahedral (3D) elements are generally used as the meshing elements.

3. Loads - Loads are usually from magnets or load carrying conductors that produce magnetic fields.

4. Boundary conditions - Following are some of the conditions that normally can be set. Magnetic insulation (no flux leaves the boundary region). Natural boundary condition (flux intersects the boundary at a right angle). Periodic and anti-periodic condition (two boundaries can be set to periodic which means that any flux leaving one of the boundaries will enter the other one). Periodic is used in machines or other devices that have symmetrical features.

5. Analysis - Solutions are obtained through solving electromagnetic equations in several iterations until they converge. 2D-problems are relatively easy to solve compared to 3D ones that can prove computationally intense. Time dependent problems/parameter sweeps require more iterations.

6. Results - Plot the parameters of interest.

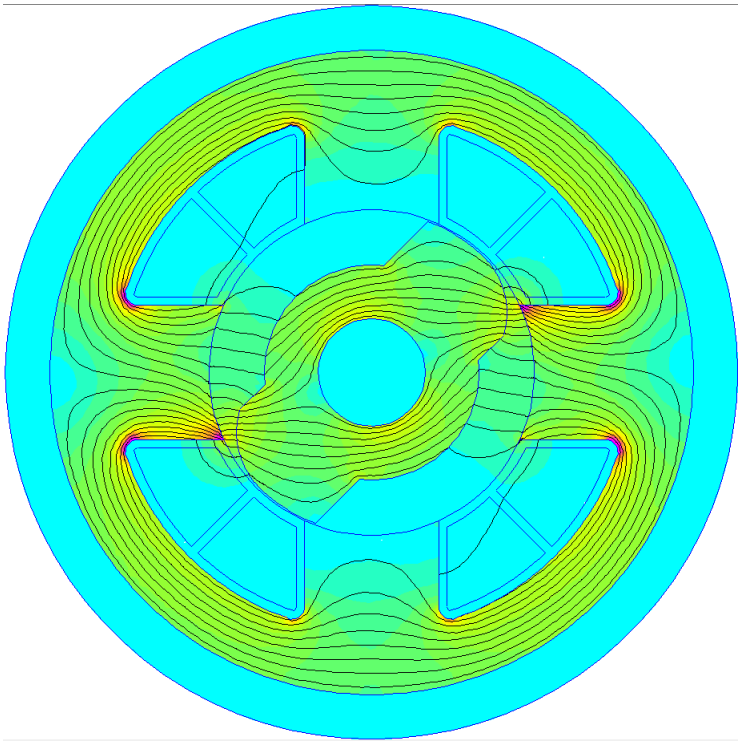

Figure 2.5: An asymmetric 4/2 SRM in FEA. Its horizontal phase is excited and torque is produced in the CW direction. The plot represents the density of the magnetic field, B. Where the lines are closer, the magnetic field is stronger.

### 2.3.3 Experimental measurement of machine characteristics

Another method of generating a machine model is by measuring the actual dynamic behavior of the machine to find the relationship between the sought-after properties. The relationship between torque, rotor position and current ($T(\theta, I)$) can be measured by fixing the rotor's position and exciting the stator with a current controller. With a constant rotor position and current, one can measure the generated torque of the machine.

Finding the relationship between flux linkage, current and rotor position ($\lambda(\theta, i)$), is more complex. This requires the machine to run so that there is a change in flux linkage, a non-zero $\frac{d\lambda}{dt}$. By integrating the voltage over one phase winding during a rotation, one can calculate the flux linkage as in equation 2.6, and thus measure how it depends on the rotor position and current. Starting from equation 2.1, the following relationship holds true for a phase:

$$U = R \cdot i + L(\theta)\frac{di}{dt} + i\frac{dL(\theta)}{d\theta}\omega = R \cdot i + \frac{d\lambda}{dt} \tag{2.5}$$

$$\lambda(\theta, i) = \int_{t0}^{t} \left( L(\theta)\frac{di}{dt} + i\frac{dL(\theta)}{d\theta}\omega \right) dt = \int_{t0}^{t} (U - R \cdot i) dt \tag{2.6}$$

### 2.3.4 Look-up Tables (LUTs)

When the machine characteristics are known, one needs to generate the look-up tables mentioned in section 2.3.1. There are two sets of LUTs, one for simulating the machine behavior, used in the dynamic model, and one used for the control system. These look-up tables are inversions between the quantities of the measured motor model. By interpolating and linearizing the measured data, it is possible to derive the relationships $\lambda(\theta, I)$ and $T(\theta, I)$.

## 2.4 Control of an SRM

Control of an SRM is in many ways different from control of other machine types such as DC- or AC-machines. The behavior of parameters such as inductance and flux are nonlinear due to the salient rotor geometry. This affects, for example, the phase currents which are typically not sinusoidal but take on more complex forms. Different speed intervals pose different challenges which are reflected in the way the control methods are designed. There are several factors that can be optimized when designing the controller. Some applications might require low torque ripple while others might require low energy usage. Not all SRM pole configurations have the same possibilities in reaching these goals. Thus, it is important to know the needs of the application before choosing a machine [1, Ch.9 pp.372-400].

### 2.4.1 Control methods

A common way of using an electric machine is as a torque source in a speed control loop. This is what is being used in BorgWarner's current BLDC solution. The speed control loop for the SRM, in a position sensor application, is seen in figure 2.6. The objective of the control loop is to deliver the correct phase voltages to the SR machine so that the reference current is flowing through the active phase, thus generating the reference torque needed to obtain a certain speed. This is done by first calculating the speed error, $\omega_{ref} - \omega_{real}$. The speed error is typically fed through a PI-controller which outputs a torque reference. Some SRMs have overlapping phase torque regions which means that several phases can be active at the same time and help produce the reference torque. In practice, SRMs with 6/4 and 12/8 pole configurations have overlapping torque regions while 4/2 configurations don't. This is because the rotor must be within 90 mechanical degrees in front of a phase for the phase to be able to exert positive torque on the rotor, and vice versa for negative torque. For a 4/2, there are only two phases which means only one phase at a time can contribute with constructive torque. See figure 2.7 for a sketch of a 4/2 SRM and its positive torque regions [1, Ch.9 pp.372-400].

For SRMs with overlapping torque regions, a torque share function (TSF) is needed. The torque share function's purpose is to decide which phases should be used to produce the reference torque and what phase currents are needed. There are several possible ways of choosing the phase currents, one way of doing it is by choosing the combination that yields the lowest copper losses, as Sjöberg described in [9]. There, the current reference LUT is modified to account for several phases producing torque at the same time for certain angles. This can be interpreted as the torque share

function being included into the current reference generator, in figure 2.6.

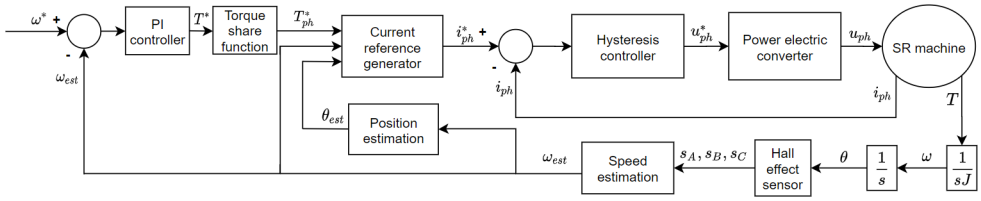


Figure 2.6: An overview of a speed control loop for a general SRM

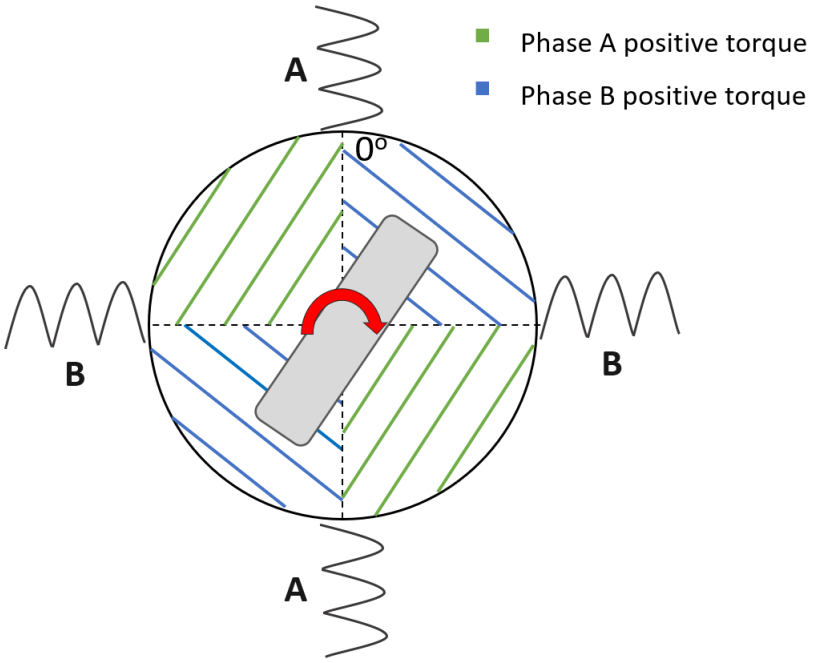


Figure 2.7: A 4/2 SRM configuration has no overlapping torque regions.

As can be seen in figure 2.6, a hysteresis current controller is used (also called direct current controller). This is due to there not being any equivalent of space vector modulation (SVM)/field-oriented control (FOC) for SRMs. In any electric machine, torque is produced only from the active phases. In an SRM, not all of the phases can be active at a time (as discussed above). This is different from the BLDC case where all phases can contribute with torque at all time by choosing appropriate phase currents (sinusoidal). In an SRM, the inactive phases' fluxes, and thus currents, must carry a zero current in order to not contribute with undesired torque. This, together with the fact that the mutual coupling between phases in SRMs is usually low, makes a hysteresis controller the natural choice for controlling the current. A hysteresis controller checks where the current is, relative to a tolerance band region. The tolerance band is defined as a certain amplitude, in positive and negative direction, from the reference level. If the current level is lower than the lower limit of the tolerance band, the current is switched on. Conversely, if the current

level is higher than the higher limit of the tolerance band, the current is switched off. A thinner tolerance band makes the current follow the reference more closely but increases the switching frequency and thus switching losses. A consequence of the machine's nonlinearity and the hysteresis controller is a variable switching frequency. The switching frequency is different for different rotor positions as well as for different speeds and current levels [6, Ch. 3.5].

To understand this, one can rewrite the voltage equation (equation 2.1) to express the time derivative of current, $\frac{di}{dt}$, see equation 2.7.

$$\frac{di}{dt} = \frac{V - iR - i\frac{dL(\theta)}{d\theta}\omega}{L(\theta)} \approx \frac{V - \epsilon}{L(\theta)} \tag{2.7}$$

A higher speed gives a higher back emf ($\epsilon$) which reduces di/dt. A certain rotor position ($\theta$) gives a certain inductance (L), where a higher one gives a lower di/dt. The current value also affects di/dt through the resistive voltage drop, a higher current leads to less rate of change.

Another concept that is relevant in SRM control is conduction angles. Conduction angles ($\theta_{on}$ and $\theta_{off}$) are used to tell the hysteresis controller at what electrical angle to activate the current for a phase ($\theta_{on}$) and when to turn it off ($\theta_{off}$). If the aim is to run the machine at higher speeds, $\theta_{off}$ needs to be decreased, since the rate of change of the current is lower at higher speeds. This is described in detail in section 2.5.1.

### 2.4.2 Speed Control

A PI speed controller can be described with the following equation.

$$T(t) = K_p\Big(e(t) + \frac{1}{\tau_i}\int e(t)dt\Big) \tag{2.8}$$

where $K_p$ is the gain (or the P-part) of the controller and $\tau_i$ is the integral time constant. A method for choosing PI-parameters is discussed in [10, Ch. 9, pp.283-285]. In short, the conclusions can be summed up in the following equations:

$$\zeta = \frac{a-1}{2} \Rightarrow a = 2.41 \,\Big|\, \zeta = 1/\sqrt{2} \tag{2.9}$$

where $\zeta$ is the damping coefficient where $\zeta = 1/\sqrt{2}$ is for a critically damped system.

$$K_p = \frac{J}{3 \cdot \tau_{filt}} \tag{2.10}$$

where $\tau_{filt}$ is the time constant of the speed filter.

$$\tau_i = 2.41 \cdot J/K_p \tag{2.11}$$

### 2.4.3 Instantaneous Torque Control

Instantaneous Torque Control (ITC) is a modern control method for Switched Reluctance Machines that utilizes the machine model. The control method produces a variable current reference during each electrical stroke. The current reference for each phase is chosen using a torque share function as described in 2.4.1. It is chosen so that the instantaneous torque, contributed by the active phases, at every position in a stroke corresponds to the calculated reference torque. A way of visualizing this can be seen in figure 2.8 where the $I_{LUT}(\theta, T_{ref})$ is used to obtain the current reference for a constant torque reference. Following these principles, an SRM using ITC can produce torque with relatively low ripple. The quality of the torque will be affected by several factors: the torque profile for each phase, the maximum current allowed, the current ripple etc [1, Ch.9][11].

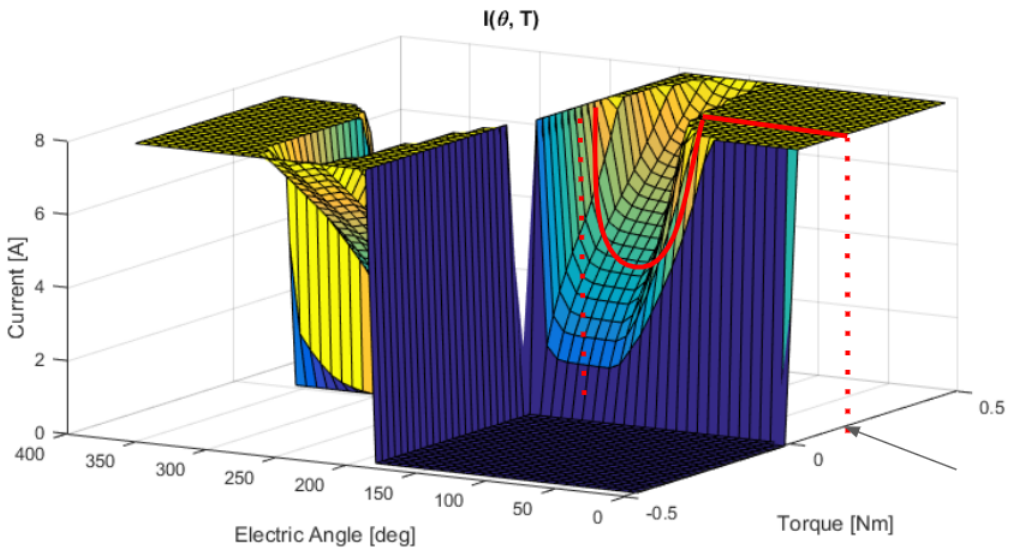


Figure 2.8: Current reference (red) for a constant torque marked by the arrow for ITC for 0-180 electrical degrees.

A 4/2 SRM (the machine considered in this thesis) has two phases. This implies that the torque regions don't overlap each other as discussed in 2.4.1. That means that the torque producing capability of the machine varies drastically over one revolution and low torque ripple is impossible to achieve in most load cases. In figure 2.9, a representative current for ITC control can be seen. The current profile is from a simulation of the thesis 4/2 machine. Note that the current reference is high close to the unaligned rotor position (0 °) and the aligned rotor position (180 °) where its torque producing capability is low.

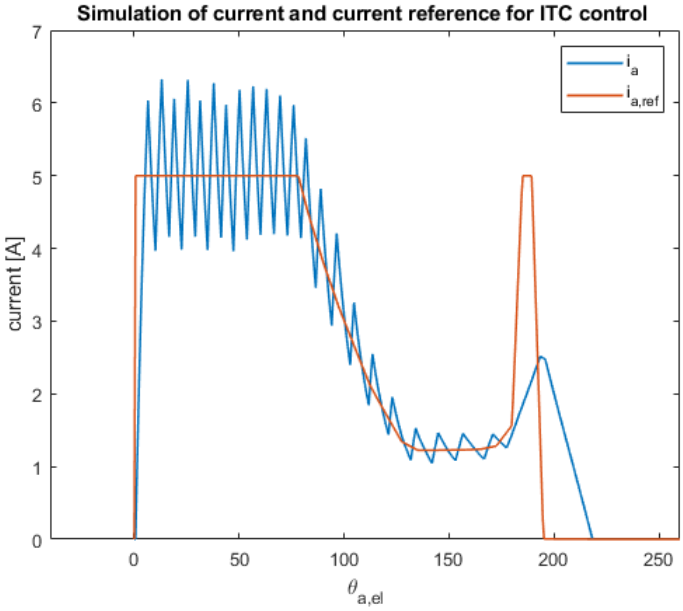


Figure 2.9: ITC current profile for phase A at 1000 rpm, $T_{load} = 0.5$ Ncm, $\theta_{on} = 0$, $\theta_{off} = 190$ electrical degrees. Current reference saturated at 5 A.

### 2.4.4 Average Torque Control

Average Torque Control (ATC) is one of the most used control methods for Switched Reluctance Machines. The control method holds a constant current reference during each electrical stroke. The current reference is chosen so that the average torque over one stroke corresponds to the calculated reference torque. Even though the current profile is much simpler than ITC, the control method still requires knowledge of the relation between control parameters such as current, commutation angles, average torque and speed [6, Ch. 5]. Some advantages and results of this control method are mentioned below.

- Since the current reference is held constant, continuous calculation of current references at each sample is reduced to once every commutation period. [12]
- ATC requires lower resolution of position estimation since the controller only needs to know when minimum or maximum inductance areas are reached. [12]
- Choosing a constant current reference during each commutation period will result in increased torque ripple. At high speeds this ripple can be filtered by the mechanical inertia of a drivetrain but can cause large fluctuations at low speeds. [13]
- ATC is preferred when utilizing the whole speed range of the machine. Since the back emf increases for high speeds and reduces the rate of current change, the ITC cannot generate its desired current profile. This is however still possible for ATC even when the machine operates in single pulse mode. [13]

The following figure shows the standard Average Torque Control method referred to in [13][14][15].

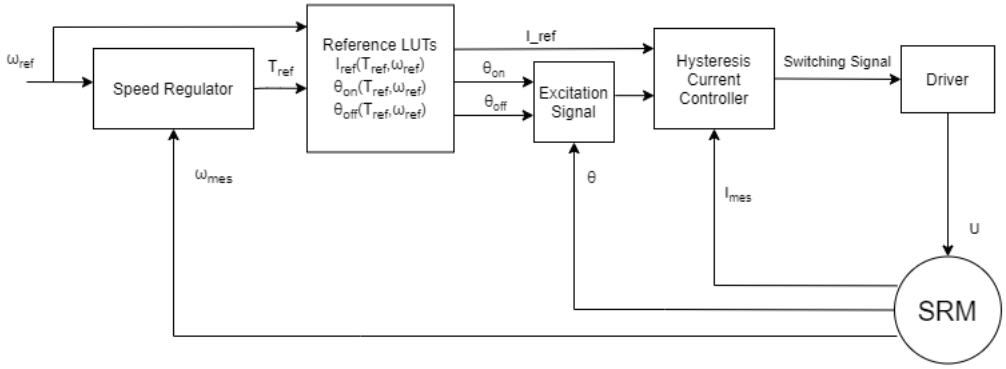


Figure 2.10: Average Torque Control Loop.

The "Reference Look-Up Tables" shown in figure 2.10 are used to find the best possible combination of the control variables $\theta_{on}$, $\theta_{off}$ and $I_{ref}$. Different combinations of these three variables can be used to reach the same torque-speed operating point, generating the same average torque during an electrical stroke. Therefore it is common to create look-up tables that are optimized to find the best set of control variables to achieve minimum torque ripple, efficiency or other optimization parameters [15][13].

To find these optimal control variables different optimization strategies such as Exhaustive Search [13][15], online-tuning [16] and Genetic Algorithm optimization [12] can be used. The figure 2.11 shows an ATC current profile during a commutation period between $\theta_{on}$ and $\theta_{off}$ with a current reference $I_{ref}$.

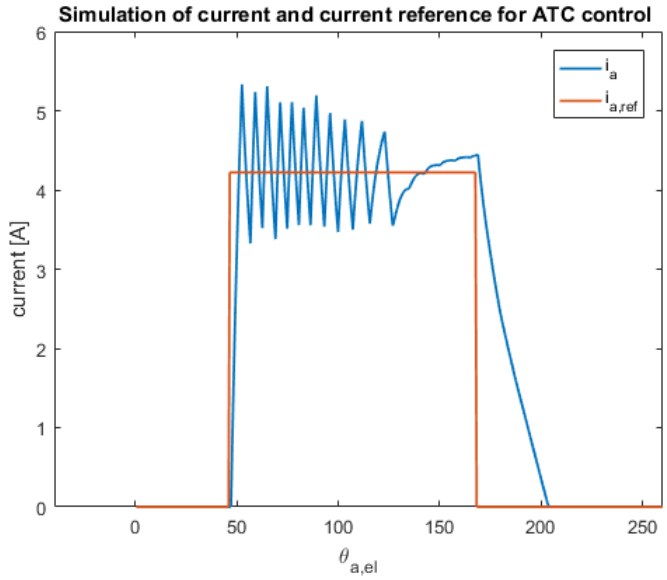


Figure 2.11: ATC current profile for phase A at 1000 rpm, $T_{load} = 0.5$ Ncm, $\theta_{on} = 47$, $\theta_{off} = 168$ electrical degrees.

## 2.5 Further improvements of SRM control

### 2.5.1 Speed Compensation for ITC

The current reference profile for a certain torque will look like in figure 2.9 for an ITC SRM. At the turn on angle for a certain phase the current should be at its peak reference value. Theoretically the current should rise instantly from zero to its peak value as soon as the rotor enters its positive torque area. But since the system is inductive, it will take a certain time to build up a current to its reference value. The speed at which the current rises is defined by equation 2.7. One can see that when the back emf increases, the rate at which the current can rise is slower. Since the back emf increases with speed, the current rise time will also increase as the SRM accelerates. Furthermore, as the speed increases, the angle which the rotor moves during a given time increases. Both these factors result in that the current will need to be turned on earlier to reach its reference in time. Since it is desirable to reach the current reference as fast as possible when the rotor is within the conduction angles, compensation for the back emf at higher speeds is required. This is done by calculating a turn on angle ($\theta_{on}$) which makes sure that the current reference is reached when entering the positive torque section.

The conduction angle can be calculated at different speeds by using back integration [9, pp. 47-50]. By finding the first current peak of the current reference profile and then integrating backwards until one has reached zero current one can find the required angle at which to switch on the phase. The backwards integration is based on the following equation.

$$v_{ph} = Ri_{ph} + \omega_r \cdot \frac{d\lambda}{d\theta_r} = Ri + \omega_r \frac{d\lambda}{d\theta_r} \approx Ri + \omega_r \frac{\Delta\lambda}{\Delta\theta_r} \tag{2.12}$$

Since the starting current $i_k = i_{peak}$ and position $\theta_k = \theta_{peak}$ is known, one can determine the starting flux linkage $\lambda_k = \lambda_{LUT}(i_k, \lambda_k)$. The change in flux linkage $\Delta\lambda_k$ is then calculated using 2.12 and thus the previous value of the flux can be determined.

$$\Delta\lambda = \frac{\Delta\theta_r}{\omega_r}(v_{ph} - Ri) \tag{2.13}$$

$$\lambda_{k-1} = \lambda_k - \Delta\lambda \tag{2.14}$$

Since the flux linkage and the position of the SRM gives a corresponding current level, one can determine $i_{k-1}$. By repeating these calculations until the current reaches zero one can find the angle at which to turn on the phase ($\theta_{on}$).

These calculations can be done for all possible torque references, both positive and negative. Note that for the positive torque references the inductance is initially very small and thus the rate at which the current may change is large according to 2.7. If the SRM is in generating mode and back integration is performed the inductance will instead be high close to $\theta_{on}$ which causes the current to rise more slowly. Therefore the turn on angle would have to be significantly earlier than in motor mode.

## 2.6 Estimating the rotor position

In order to control an SRM, the position of the rotor, $\theta$, needs to be known or estimated at all times. This is crucial in order to calculate the current reference, $i_{ref}(\theta, T_{ref}, \omega)$ and the flux linkage, $\lambda(\theta, i)$ which is done using look-up tables. The position data is also used to calculate the speed, which is used for speed control and for speed compensation as presented previously in section 2.5.1. The rotor position can be read using a Hall effect sensor or an encoder, for example, or estimated with any of the methods described below.

### 2.6.1 Sensorless

Sensorless position estimation of the rotor can be implemented to remove the cost and packaging requirements of a position sensor. Because some of the SRM's magnetic attributes such as flux linkage and self-inductance are position dependent, the position can be estimated by knowing these entities. As such, there are several methods that have been tested for estimating the rotor position; Self-induction, Flux-based estimation, Observer-based, Inductance inflection point based and Neural Network based position estimation are just some examples. Below, the Self-inductance method and the Flux-based estimation method are described. [1, Ch. 11][17]

#### Self-inductance method

By observing the change of the slope of the current, between two switching periods, it is possible to estimate the self-inductance for the given current level and rotor position. Because self-inductance is a function of phase current and rotor position, the rotor position can be estimated by measuring the current and estimating the self-inductance. This method is good for low speeds since resistance is not used in it and resistance variation during an electric stroke is not a problem. A varying resistance can be especially problematic in the Flux-based estimation method at low speeds where the voltage is integrated over a longer time. The lower the speed the more likely it is that the resistance is incorrect for some parts of the period. This error gets integrated and leads to an incorrect flux estimation and thus position estimation. The self-inductance method works better the more change in inductance there is for a position increment. This means that it is unsuited to use near unaligned rotor position where the inductance curve is almost completely flat. This isn't a problem in a machine using three or more phases. For every rotor position there is always at least one phase that is in a good position, relative to the rotor [1, Ch. 11].

#### Flux-based estimation

One common way of estimating the position without a sensor is by estimating the flux linkage. By inverting the current LUT, $i(\theta, \lambda)$, to have the form of $\theta(i, \lambda)$, one might believe that it is possible to know the position for every current and estimated flux level. This is, however, not possible, since the inductance can have the same value for two different angles. Instead, by comparing the estimated flux

linkage of the machine with a reference flux linkage, defined at the turn off angle, one can identify when the estimated flux linkage reaches the reference level. When the reference flux linkage is reached it means that the rotor has reached the turn-off angle. The reference value is precalculated and stored in a look-up table and has the following form:

$$\lambda_{ref}(i_{phase}, \theta_{off} = const) \tag{2.15}$$

The estimated flux linkage is calculated as in equation 2.6 for a phase:

$$\lambda_{ph}(\theta, i_{ph}) = \int_{t_1}^{t_2} (u_{ph} - R_{ph} i_{ph})\, dt$$

which becomes the following in discrete time:

$$\lambda(k) = \lambda(k-1) + \Big(u(k) - R(k) \cdot i(k)\Big) T_s \tag{2.16}$$

Implementing this method allows the position to be known at $n$ positions during a revolution where $n$ is the number of stator poles. This allows speed and position to be estimated over the full revolution. Furthermore, it implies that the method works better at high speeds than at low speeds. This is because more position estimations are obtained per time unit [18][19].

### Error estimation of resistance

Assuming that the phase voltage and current were measured without error, the only source of error for estimating the flux linkage is the phase resistance. The resistance of a phase winding changes with the temperature. When the current is 0, the flux linkage should be 0 as well since $\lambda = L(\theta)i$. If the flux linkage is above 0 at that point, the resistance estimation was too low and vice versa and gets adjusted. This difference in flux linkage is called the flux linkage error, $\lambda_{err}$. This can be used to tune the resistance parameter during operation to better estimate the flux linkage according to the following expression [19][20, pp.19-21].

$$\lambda_{err} = \int_{t_1}^{t_2} -R_{err} \cdot i_{ph} dt \Rightarrow R_{err} = -\frac{\lambda_{err}}{\int_{t_1}^{t_2} i_{ph} dt} \tag{2.17}$$

Resistance estimation is also possible in PMSM machines as proven in [21]. There, a model reference adaptive system (MRAS) estimator is used in order to drive the machine without a position sensor. Extended Kalman Filters (EKF) have also been proposed as seen in [22] and [23].

## 2.7 Power electronic converters

A power electric converter is usually used to convert power from DC-AC, AC-DC, DC-DC or AC-AC. It contains power semiconductors, such as power transistors and power diodes, inductors and capacitors and converts power by switching the transistors in a controlled manner. In an SRM, the current waveform will depend on the dynamic model and won't typically have the shape of a DC or AC current. The current reference generator LUT can be used to visualize it, see figure 4.13 for an example.

In contrast to AC machines (ACM), the torque direction of the SR machine is not dependent on the direction of the current. Instead, it depends on the electrical angle (positive torque from about 0 to 180 electrical degrees and negative from about 180 to 360 electrical degrees). Whereas a four-quadrant converter is usually used for an ACM, a two quadrant-converter is usually used for an SRM. Because of this, the converter looks different in an SRM than in an ACM. Some different converter layouts are described below.

The design of SRM converters make them fault tolerant, if one phase would break the others could still continue to operate independently. This is not the case in a typical ACM converter where the three windings share a common neutral point [1, Ch. 10].

### 2.7.1 Asymmetric bridge converter

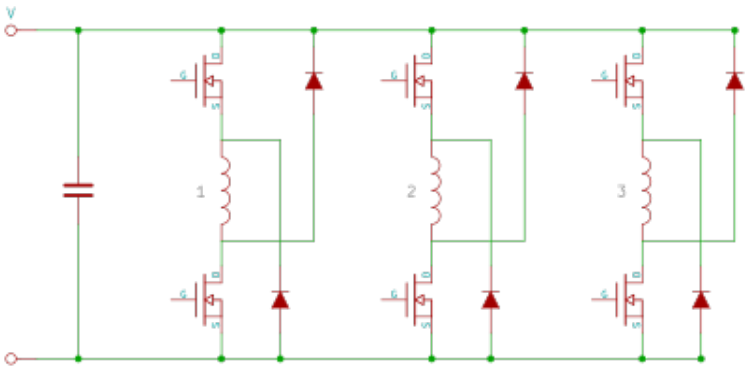


Figure 2.12: The asymmetric bridge converter layout for a three phase machine.

The asymmetric bridge converter is the most commonly used converter layout for SRMs. It uses two power transistors and diodes for each phase, which is relatively many, which means it might not be cost effective for smaller applications. It is the same amount, however, as a typical two-level converter used for AC machines. One advantage with the asymmetric bridge converter is that it can be built using widely available H-bridges. One H-bridge can power one phase using only T1, T4, D2 and

D3. It has three different operation modes for each phase and is typically being used together with a hysteresis current controller.

The first mode is with both transistors on, this puts $V_{DC}$ over the phase winding, making the current increase rapidly until it hits the upper current reference limit. This mode is sometimes called magnetizing mode. The second one is with both transistors off, this puts $-V_{DC}$ over the phase winding, making the current decrease rapidly until it hits the lower current reference limit. This mode is sometimes called demagnetizing mode. The third one is when the upper transistor is on and the lower one is off; this makes the current freewheel through the inductance and the diode. The phase winding voltage is equal to the voltage drop over the diode and transistor and so the current drops slowly (compared to the other modes). Using only the first and second mode is called hard switching and also using the third mode is called soft switching. Soft switching requires less switching since the current decreases more slowly [1, Ch.10, p.426].

### 2.7.2 Other converter types

There are other types of converters suitable for SRMs that have their own pros and cons. For example, some of them are built to try to reduce costs by sharing transistors in between phases, thus reducing the number of total transistors. Worth mentioning are the (N+1)-switch converter, the C-dump converter, the Split DC-converter and the Split AC-converter [1, Ch. 10]. Below in figure 2.13 three of the mentioned converter variants are pictured.

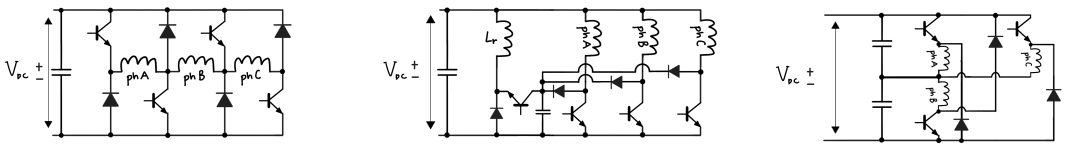


(a) (N+1)-switch converter (b) C-dump converter (c) Split DC-converter

Figure 2.13: Three SRM converter variants.

# Chapter 3

# Design and implementation of controller

## 3.1 Machine selection

The goal, when deciding on a machine to evaluate, is to find the one that best resemble the existing machine (a ∼150 W 6/4 BLDC). However, in the commercial market, there were not many available SRMs in that size range. The machine that was selected is a HishineTech model HSSRM-52F-70350. It is a 4/2 SRM with 700 W rated power and 35 000 rpm rated speed when fed with 300 $V_{dc}$. It is specified for a maximum current of 5 A. 5 A is consequently used as a saturation value for the current controller.

## 3.2 Used nomenclature

Clockwise direction (CW) was chosen as positive direction since this is the spinning direction for which the machine was designed. Aligned position relative to phase A and unaligned position relative to phase B is displayed in figure 3.1. Some electrical angles for each of the phases are also shown, in corresponding colors. Notice that 360 electrical degrees corresponds to 180 mechanical degrees. The relation between mechanical and electrical degrees can be seen in the following equation.

$$\theta_{el} = N \cdot \theta_{mech} \tag{3.1}$$

where N is the number of pole pairs. In the 4/2 SRM, N = 2 due to there being 2 stator pole pairs. 0 electrical degrees, for each phase, is defined as the unaligned position and 180 electrical degrees is defined as the aligned position.

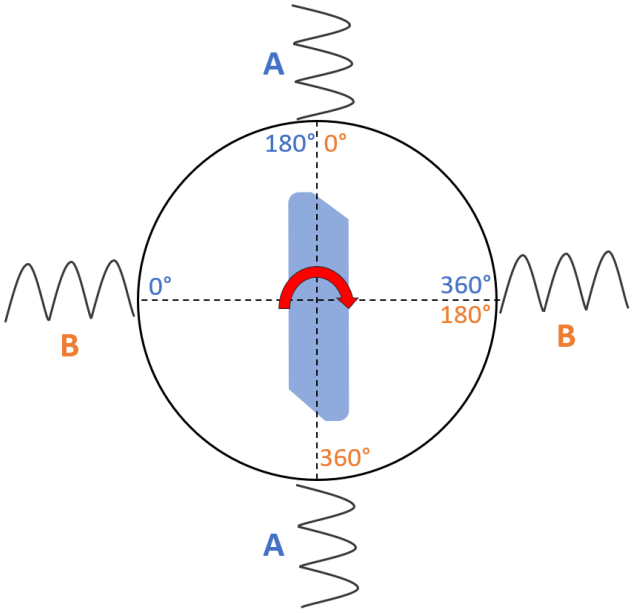


Figure 3.1: Coordinate system used in the thesis.

## 3.3 FEA modelling of machine

As previously stated in 2.3, there are two ways of creating a machine model. One of the methods requires measurements on a running machine which can't be realized until a current controller is in place. Because of this, an approach was devised to first use the FEA calculations to generate a machine model, then implement a speed controller on it in Simulink and lastly verify the FEA machine model through direct measuring on the machine. The purpose of the verification is to compare the initial LUTs obtained through FEA with those obtained from measuring on the machine and correct the LUTs accordingly. The goal here being to find the LUTs that best represent the machine, in order to control it optimally.

An FEA was made by Avo Reinap, assoc. professor at IEA (industrial electrical engineering and automation), who assisted us in the project. To properly be able to model the machine, one of the three machines that had been acquired was disassembled and measured. The software used for the analysis was FEMM, an open source program widely used for electromagnetic FEA. The following geometry, materials and settings were used:

### Geometry

The geometry shown in figure 3.2, is the one measured by Avo Reinap.

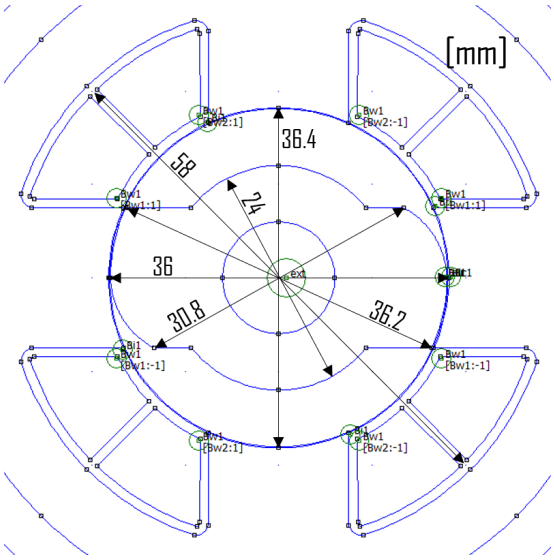


Figure 3.2: Key dimensions used in FEMM.

### Materials

Figure 3.3 shows which materials were used in the FEA. Note that the material data was guessed since no specifications were available from the supplier. Table 3.1 explains what the different labels mean.

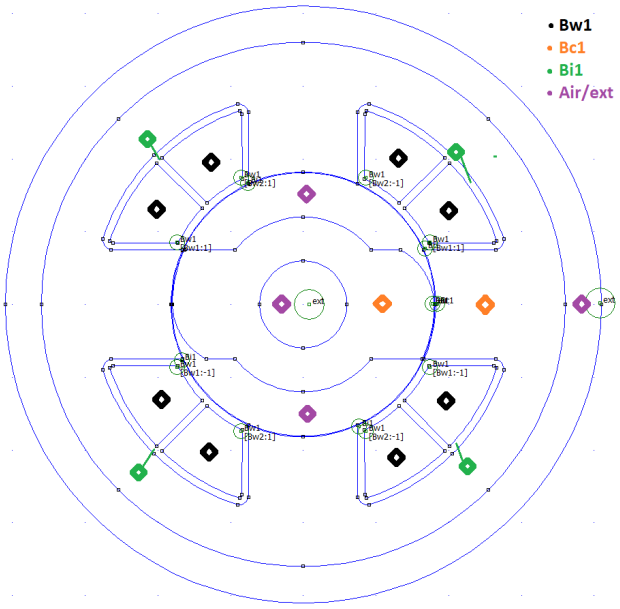


Figure 3.3: Machine shown with materials used in FEMM.

| Label | Material | Rel. $\mu_{x,y}$ | B-H curve | El. cond. [MS/m] | Lamination & wire type |
|---|---|---|---|---|---|
| Bw1 | Cu | 1 | Linear | 57.143 | Not stranded |
| Bc1 | Fe | 3315.9 | Nonlinear | 1.818 | Laminated in-plane |
| Bi1 | Plastic | 1 | Linear | 0 | - |
| Air/ext | Air/plastic | 1 | Linear | 0 | - |

Table 3.1: Materials used in FEMM.

**Settings**
The following settings were set under problem definition:

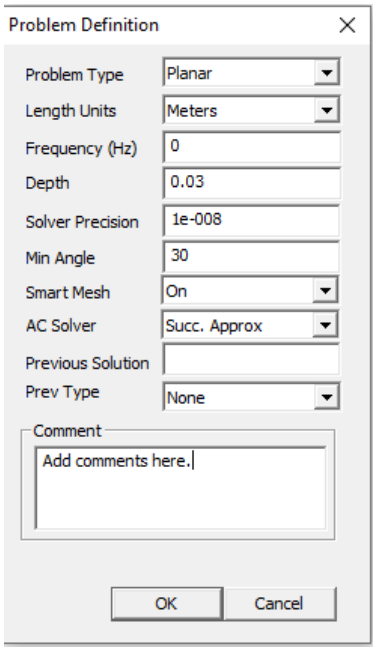


Figure 3.4: FEMM simulation settings.

By sweeping the rotor position and current level in one phase (the other phase was set to 0 A), torque and flux linkage data was obtained for all the operation points of the machine. This was put into two LUTs; $T(\theta, I)$ and $\lambda(\theta, I)$ for the torque and flux linkage data, respectively. Rotor position was swept in intervals of 7.5° mech. and current in 50 At (ampere-turns). Because current was simulated in ampere-turns, a scaling by the number of phase turns needs to be applied afterwards to get correct current and flux linkage values. With the results of the FEA it is possible to create the look-up tables necessary to build a machine model and to implement control methods. Since $\lambda(\theta, i)$ and $T(\theta, i)$ were obtained, it is necessary to invert them in order to obtain the LUTs that can be used to predict the machine's behavior such as $i(\theta, T)$ and $i(\theta, \lambda)$. The LUTs and their inverted versions can be seen in figure 4.2 in the results.

## 3.4 Microcontroller and power stage

In this master thesis, the microcontroller being used is a MicroAutoBox 1513/1514 and the power stage is a RapidPro Power unit with two of the PS-HCHBD 2/2 module, both from dSPACE. The microcontroller's task is to read sensors and update reference values while the power stage should deliver the requested voltage and current to the phase windings of the SRM. The MicroAutoBox (MAB) combines the advantages of a rapid prototyping system with those of an automotive electronic control unit (ECU). Because of this, it is well suited for automotive prototyping. The MAB in this thesis is equipped with an FPGA that enables flexibility and fast communication with the power stage. To enable running the machine with only the default MAB, the FPGA unit is not used in this thesis. The MABs software is integrated into MATLAB and code can easily be generated from Simulink models. This code can then be uploaded to the MAB in an intuitive way, using dSPACE's ControlDesk. ControlDesk enables the user to monitor and log signals from the Simulink model. It also allows live editing of Simulink parameters such as gains and control parameters, which is especially useful in tuning and testing. The MAB has a high number of input/output ports with which it communicates with the Hall effect sensor and the power stage. During a time step, $T_s$, the MAB gets position sensor input from the Hall effect sensor and current readings from the RapidPro. Afterwards, it executes the control loop which results in a new current reference. The MAB then outputs the corresponding switching signals back to the RapidPro's MOSFETs which results in a current change in the SRM's phase windings.

The RapidPro contains two rails that can each hold a power stage module. In this case it houses two PS-HCHBD 2/2 modules; they are high current, double half-bridges for driving loads in different modes in 12 V or 24 V power supply systems. In total it means that the RapidPro contains two H-bridges. This means that it can be used to create an asymmetric bridge converter layout for a two-phase machine. The RapidPro can set the two modules in several different modes and in this case the mode that is used is "electric drive, two half-bridges". It is chosen since the setup is used when driving inductive loads, according to the data sheet. When using these modules as an asymmetric bridge converter, the two phases operate like in figure 3.5.

## 3.5 Simulink modeling

### 3.5.1 Control system overview

With the goal of comparing the chosen SRM with the existing BLDC solution, it was decided to control it using a speed controller. It was also decided to only design control methods for motoring purposes which corresponds to their current pump application. Therefore, generative machine control was deemed to be out of scope for this thesis. Due to the chosen machine being a 4/2 SRM, there was no need to implement a torque share method as described in section 2.4.1. This simplifies the control scheme slightly, see figure 3.6. To further mimic the existing solution, a DC-link voltage of 12 V was chosen. A maximal switching frequency of 20 kHz was used, both in simulations and the real-time applications as the BLDC switches at

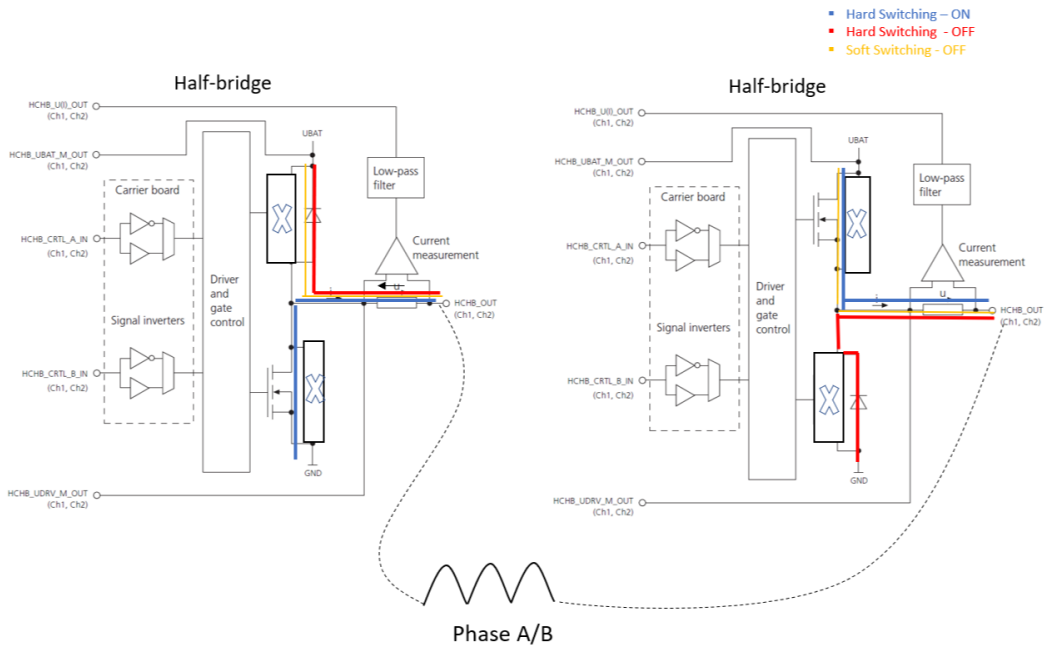


Figure 3.5: Operating modes of both modules of the asymmetric bridge converter.

20 kHz.

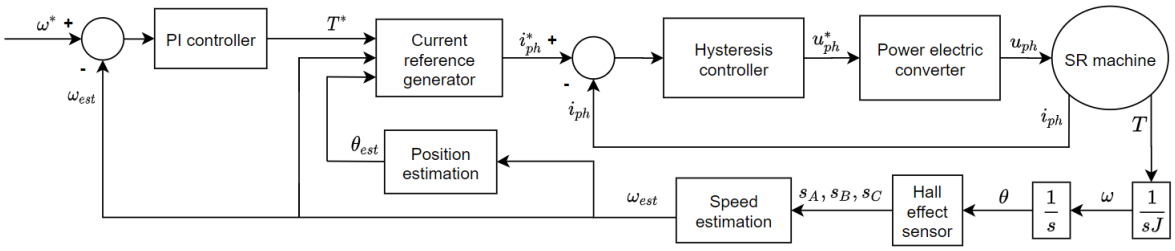


Figure 3.6: The simplified speed control loop for the 4/2 SRM.

It was decided to implement ITC and ATC control to fulfill the goal of implementing two control methods. It was believed that they could be implemented in the limited time of the thesis and provide adequate performance as well as interesting insights into SRM control. It was also decided to implement a simple sensorless position estimation algorithm. Due to time constraints, it was only successfully implemented in Simulink simulations, and not in the real-time application.

### 3.5.2 Model explanation

In Simulink, a simulation model for ITC was first constructed, see figure 3.7. The simulation model contains all the necessary parts for simulating the running machine. Afterwards, a simulation model for ATC control was made, based largely on the same model.

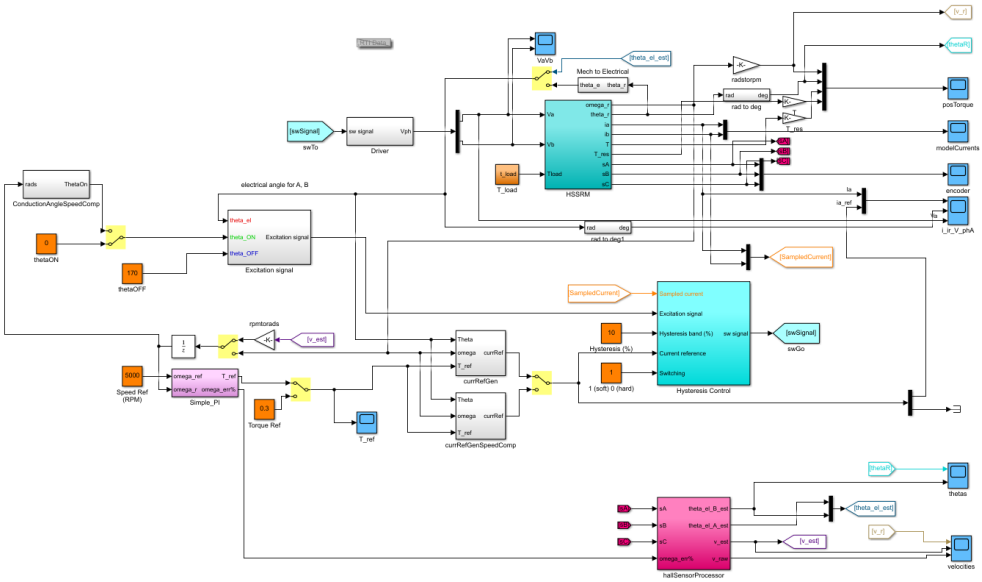


Figure 3.7: The Simulink simulation model.

The key parts of the simulation model are the following:

- The SRM machine model ("HSSRM")
- The excitation signal block
- The hysteresis current controller
- The power stage ("Driver")
- The current reference generator
- The Hall sensor processor
- The speed controller
- The speed compensation feedback

When the simulation was working satisfactory, the same models were used to create the real-time models. This is done by replacing the SRM machine model, power stage and Hall effect sensor blocks with corresponding inputs or outputs to the RapidPro and the position sensor. The time step in the real-time application was first set to $T_s = 1/F_s = 5e - 5$. This, however, led to overrun when executing the code (the microcontroller couldn't execute the code quickly enough). To solve this, a part of the code was set to run at 10 kHz. This part is the segment that handles updating reference values. The code that still runs at 20 kHz is the code that reads the phase current and updates the switching signal. Below, each key part of the model is described briefly.

**SRM machine model**
It works like the flowchart in figure 2.3. It uses the two look-up tables ($I(\lambda, \theta)$ and $T(\theta, I)$), obtained from the electromagnetic FEA, to calculate the current and torque from each phase. Additionally, it calculates the acceleration, velocity and position of the rotor by comparing the produced torque with friction and load torque. This part of the model is in continuous time since it, in the real-time application, is replaced with the real machine which of course operates in the continuous time domain.

**Excitation signal block**
Checks if any of the electrical angles of the phases are within a region where the current should be enabled. This region is from theta on to theta off, usually about $0°$ to $180°$ but can be changed for example when using speed compensation. The excitation signal that is produced is effectively used to turn on and off the current controller.

**Hysteresis controller**
If enabled, checks if the current is within the tolerance band of the reference value. If it is lower than the lower tolerance band, the switching signal (for that phase) is a 1 (called "hard on" in the converter theory section). If it is higher than the upper level, the switching signal is either a 0 or -1, depending on the switching mode (0 for "soft off" and -1 for "hard off"). The switching signal is then output to the power stage. The controller also has a form of hysteresis logic; if the current is rising/falling but is within the tolerance band, it is allowed to continue to do so.

**Power stage**
Receives the switching signal from the current controller and outputs the corresponding voltages for each phase respectively. In the real-time application it outputs digital signals to the MOSFETs of the RapidPro.

**Current reference generator**
The current reference generator takes rotor position and torque reference as input and outputs a current reference. The inverted torque LUT, $i_{ref,LUT}(\theta_{el}, T_{ref})$, is what links the torque reference together with the current reference. As mentioned earlier, no torque share function is needed and so the torque reference directly gives the reference torque for the active phase. There is also the speed compensated current reference generator which is described in section 3.5.5.

**Hall sensor processor**
The Hall sensor processor block processes the signal from the Hall-effect sensor and outputs rotor position and speed. This is described in detail in section 3.5.4.

### 3.5.3 Simulink settings

In the simulation model, the solver is set to the type: fixed-step, solver: automatic. This is due to the model containing both discrete and continuous parts. The rest of the settings are set to default. The fixed-step size is set to $T_s = 1/20000$. In the real-time model, the solver type is changed to discrete (no continuous states). This is because without the SRM block, no continuous states are needed.

### 3.5.4 Position estimation with Hall-effect Sensor

#### With a position sensor

The SRM used in the thesis is equipped with a rotor position sensor. The sensor consists of three Hall effect sensors (A,B,C), ∼120° apart, and a 4-pole magnet ring on the rotor axis, see figure 3.8.

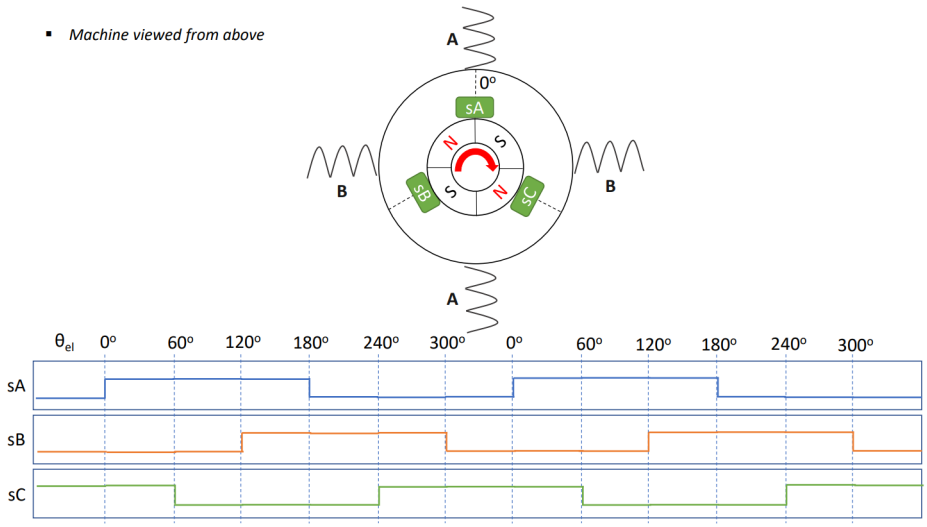


Figure 3.8: The Hall effect position sensor.

The Hall effect sensors are unipolar, which means that they are high (1) close to north and low (0) close to south. Every sensor is either high or low for a quarter of a rotation (90° mech./180° el.) which can be seen in figure 3.8. This gives a precision of $\theta \pm 15$ ° mech. at any given point in time. The only position where the angle is better known is at a flank (where one sensor value goes from high to low or low to high). The rest of the angles need to be estimated. This can be done by estimating the speed and then using it to calculate how much the angle will change during a sample time ($T_s$). The speed also needs to be estimated since the only speed that actually can be calculated is the average speed between two flanks. There are several ways of estimating the speed; A weighted filter or projection using the two last average speeds are just two examples. The following equation shows the new speed being calculated with the weighted filter method.

$$\omega_{est} = \sum_{i=m-n}^{m} \alpha_i \omega_i \tag{3.2}$$

where $\alpha$ is the weight of a sample, $m$ is the index of the last average speed value, $n$ is the number of samples to filter on. $n = 9$ is chosen and $\alpha = [0.21, 0.185, 0.16 \ldots 0.02]$. $n = 9$ is chosen because in this case it results in a good trade-off between filtering the signal well and not delaying it too much. Using this, the rotor position can be updated at a time step using the following equation:

$$\theta(k+1) = \theta(k) + \omega_{est} \cdot T_s \tag{3.3}$$

### Position signal interpretation logic

The Hall sensor processor block takes the three hall effect sensor signals from the position sensor and uses them to estimate position and speed as demonstrated above. Three different types of look-up tables (LUTs) are used to interpret the sensor signals; one for "no speed position", one for "rotation position" and one for deciding the rotational direction. The "rotation position"-LUT comes in two different versions, one for clockwise (CW) and one for counter clockwise (CCW) rotational direction. The LUTs are all of 2x2x2 size, where each of the three dimensions correspond to the three sensor signals; $\bar{s}$ = [sA, sB, sC]. The "no speed position"-LUT outputs the electrical angle that is in the middle of the two closest flanks if the rotor speed is 0. For example: $\bar{s}$ = [1,0,0] is closest to the 60° and 120° flanks so 90° is output. The "rotation position"-LUT outputs the electrical angle of the last flank read. The "rotation position"-LUT's angle output is the one that is used to calculate the average speed between two flanks. The "rotation position"-LUT for CW-direction can be seen in table 3.9

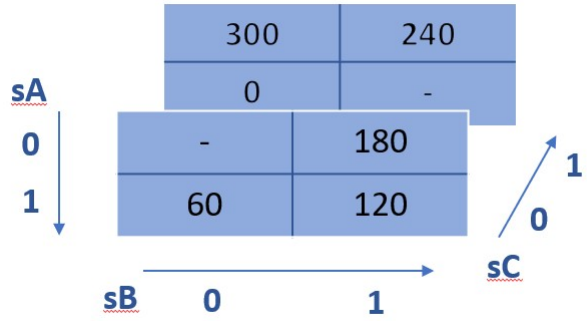


Figure 3.9: "Rotation position"-LUT for CW rotation (2x2x2 matrix).

Rotational direction is decided on a flank by comparing the new sensor output, $\bar{s_1}$, with the previous one, $\bar{s_0}$. The difference, $\bar{ds}$, is multiplied with a vector, $\bar{v}$ = [1, 2, 3], giving $\bar{ds} \cdot \bar{v} = [1 \cdot ds_a, 2 \cdot ds_b, 3 \cdot ds_c]$. The resulting vector is then summed giving $1 \cdot ds_a + 2 \cdot ds_b + 3 \cdot ds_c$. Since only one of the sensor outputs change per flank, only one of $[ds_a, ds_b, ds_c]$ is non-equal to 0. This sum is then compared to the output value of another LUT, seen in figure 3.10. The output of the LUT corresponds to the sum $(1 \cdot ds_a + 2 \cdot ds_b + 3 \cdot ds_c)$ at the new flank for clockwise direction. This LUT looks different for counter clockwise rotation and so this LUT can be utilized to differentiate between the two directions. If the two signals are the same, it means that the rotor is spinning clockwise and vice versa. The Simulink implementation of the rotational direction algorithm can be seen in figure 3.11.

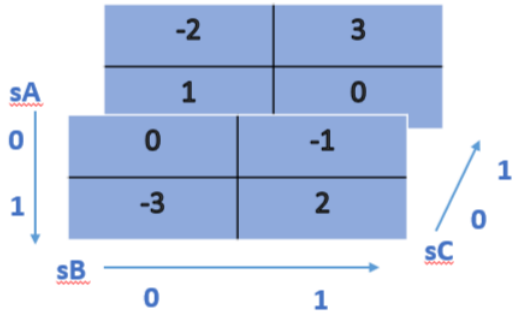


Figure 3.10: LUT used to decide rotational direction.

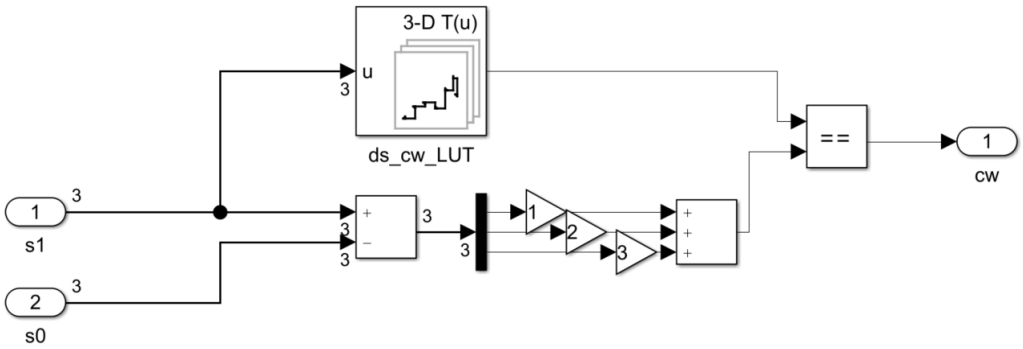


Figure 3.11: Rotational direction logic.

### 3.5.5 Speed compensation

Speed compensation was implemented to allow the ITC to reach its initial current reference in the beginning of the electric stroke. As explained in 2.5.1, the phase is turned on earlier at higher speeds due to back emf affecting the time derivative of current, see 2.7. This means that the turn on angle, $\theta_{on}$, depends on the speed. The back integration method used in [9] and described in 2.5.1 was used to create new look-up tables for the current reference generator. Speed compensation was performed at speeds between 500 rpm to 4000 rpm and implemented in the Simulink model as a separate current reference generator block. See figures 4.3, 4.4, 4.13 and 4.14 in the results for the speed compensated look-up tables. For ITC, the turn off angle, $\theta_{off}$, is kept constant. It is set to $\mp 15$ electrical degrees (CW/CCW) relative to where the torque is 0 near the aligned position (about 180° depending on the LUT).

### 3.5.6 Sensorless position estimation

BorgWarner's current BLDC actuator is run sensorless in many of their applications. In this thesis, it was decided to implement a simple sensorless ITC position estimation based on the flux-based estimation principle. This method was chosen because it was considered achievable in the limited time frame of the thesis; it is a relatively easy method to implement and parts of the code can be reused in this

implementation (such as the Hall sensor processor block).

The implemented sensorless position estimation method consists of two parts; a start-up sequence and an operation mode. The start-up sequence's purpose is to start the rotor from any given position in the desired direction. The operation mode estimates the position when running the machine. In this implementation, the start-up sequence first identifies which of the phases that is closest to the rotor. This is done by sending short voltage pulses through the phases and measuring the resulting phase currents. The phase with the lowest current has the highest inductance (see equation 2.7), which means that phase is closest to the rotor.

The rotor is then "locked" into the closest phase by activating it at 3 A for a set time of one second. Due to the rotor's asymmetry, the "locked" position is not exactly aligned with the phase but offset some degrees, see figure 3.12 for a rough sketch. 3 A turned out to be a good level for this motor; a higher current attracts the rotor more quickly but risks creating oscillations in the rotor which would make its position uncertain. The reason the rotor is "locked" into a phase is because it enables the rotor to start spinning in either direction afterwards by using a predefined current sequence.

A start-up sequence can look as follows: The machine excites phase A and B with short voltage pulses. The currents are measured and phase B has higher current than phase A. This means that the rotor is the closest to phase A and so phase A is turned on at 3 A for one second. The rotor is now in the "locked" position. To then start spinning in either direction, phase B must be turned on first (since turning on phase A would do nothing). This pulls the rotor in the CW direction. If the desired rotation direction is CCW, the current in phase A is activated after some 30-50°and the rotor switches direction. After a pre-decided time, the phase is switched again (in both cases) to give the rotor additional speed in order for the estimation method to start working better.

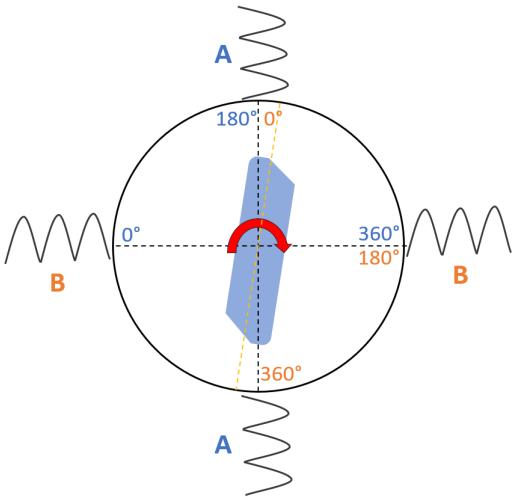


Figure 3.12: The "locked" position for phase A, the position where the rotor has the least reluctance relative to the active phase.

If the machine would be a 6/4 with overlapping torque regions, start-up would be easier since the rotor could be made to spin in either direction directly by activating the closest phase in the desired spin direction. With the 4/2 SRM, enough torque can't be produced to overcome rotational friction at low and high electrical angles ($\theta_{el} \lesssim 60$ and $\theta_{el} \gtrsim 300$). This means that for certain rotor positions, it is only possible to spin the rotor one way, to the closest phase. To start the rotor, different current sequences are used for CW and CCW. These currents were found by starting the machine from the "locked" position in CW and CCW direction and observing the currents the controller sent to the phases, and then copying them. After these current pulses have given the rotor a starting speed, the machine's sensorless position estimation works well enough to run on its own and so the machine is switched to that mode, operation mode.

After locking in, operation mode is turned on and flux linkage estimation is started. The estimation is based on the method described in the theory section. The flux linkage for each phase is estimated by integrating the active phases' voltages. When the estimated flux linkage reaches the reference flux linkage level, defined by the $\lambda_{LUT,ref}(i_{ph}, \theta_{off} = const)$, it counts as a flank. The flank is treated in the same way that a flank from the Hall sensor is, except for there now being four flanks for every full rotation (one for each stator pole) instead of 12. At a flank, the average speed is calculated from the last flank and used to estimate the position in between flanks. The position is updated when a flank is encountered (to $\theta_{off}$ for the active phase).

In normal operation, the two phases should take turns generating flanks. Two flanks, or more, could be generated in a row, by mistake, by the same phase because of current oscillations causing oscillations in the flux estimation. The estimated flux can at one moment become larger than the reference, and generate a flank, only to in the next moment oscillate below the reference and then create another flank once it grows larger than the reference. To avoid this, one phase must wait for the other phase to generate a flank before it can do so itself again.

In the beginning of the development of the operation mode, the flux linkage position estimation is run in the background in simulations. This is done while the SRM is controlled using the real rotor position and speed. This method is chosen in order to bug test the code more easily and more quickly reach a working solution. Some results of these tests are presented in the results, section 4.6.

### 3.5.7 Speed Controller

The PI-controller was implemented with anti-windup in Simulink. Anti-windup is achieved by saturating the integrator part to the maximum torque the machine can theoretically output. The parameters are first set to the theoretical values and then iterated by hand to reach better performance. Better performance in this case being quicker step times, quicker stabilization time etc.

## 3.6 Optimization of ATC control variables

Since several combinations of the ATC control variables $\theta_{on}, \theta_{off}, I_{ref}$ can operate at the same operation point in the torque - speed plane an optimization strategy is required to implement the control method. The optimization strategy chosen is known as "Exhaustive Search" and is commonly used in ATC optimization. The method was chosen due to its simplicity and made it possible to quickly set up an optimization. The goal of the optimization, in terms of machine performance, is to minimize the produced torque ripple and thus the speed ripple while having minimum losses. Due to the 4/2 configuration of our machine another optimization parameter, speed ripple, was also implemented as an alternative to torque ripple. Since the 4/2 configuration of the chosen machine does not have the possibility to produce a driving torque throughout one entire electric stroke, its torque ripple is by default high. Therefore, the alternative optimization parameter "speed ripple" is used to measure control performance. The optimization problem is multi-objective oriented since a minimum torque ripple (or speed ripple) requires a different set of control variables than minimum losses does. The optimization strategy developed is based on the ones presented in [12][14].

The torque ripple is defined as in the following equation. Where $T_{max}$ and $T_{min}$ are the maximum and minimum torque during one electrical stroke.

$$T_r = \frac{T_{max} - T_{min}}{T_{mean}} \tag{3.4}$$

Speed ripple is defined as the Root Mean Square (RMS) value of the speed error when the simulation has reached steady state. This definition is used to take both the size of oscillations and possible offset errors into consideration. In the following equation $S_r$ is the RMS speed ripple, $e$ is the error of the actual speed and reference speed and $n$ is the number of samples.

$$S_r = \sqrt{\frac{e_1^2 + e_2^2 + e_3^2 + ... + e_n^2}{n}} \tag{3.5}$$

The copper losses are used as an indicator for efficiency where the calculated losses, $E_{loss}$, are defined as the following. $T_{ElectricalStroke}$ is the time in which the phase is active during an electrical stroke.

$$E_{loss} = R_{stator} \cdot I_{ref}^2 \cdot T_{ElectricalStroke} \tag{3.6}$$

The weights $w_r$ and $w_{cu}$ are used to weigh the cost of torque or speed ripple versus copper losses and are defined as the following.

$$\begin{aligned} 1 &= w_r + w_{cu} \\ 0 &\leq w_r \leq 1 \\ 0 &\leq w_{cu} \leq 1 \end{aligned}$$

Base values $T_{br}$, $S_{br}$ and $E_{bcu}$ are defined as the minimum torque ripple, speed ripple or copper loss found for a certain combination of the control variables at

a torque-speed operating point. The multi objective function is then defined as in equation 3.7. For the 4/2 machine in this thesis, speed ripple is used but in another configuration it can be replaced by corresponding torque ripple variables, as discussed above.

$$F_{obj}^{opt}(\theta_{on}^{opt}, \theta_{off}^{opt}) = min(w_r \cdot \frac{S_r}{S_{br}} + w_{cu} \cdot \frac{E_{cu}}{E_{bcu}}) \tag{3.7}$$

Figure 3.13 illustrates the optimization algorithm used.

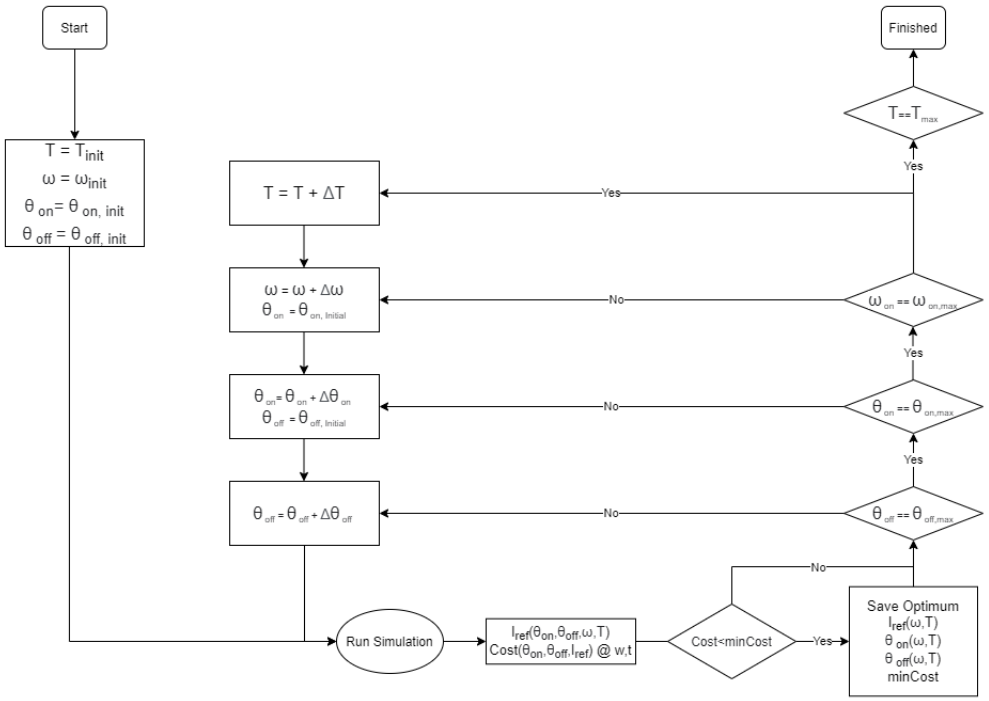


Figure 3.13: Flow chart of the exhaustive search algorithm.

The optimization is run over different combinations of torque loads and speed references in the machine's torque-speed plane. For each operating point, optimal control variables are found and stored in reference look-up tables. If the operating point is outside of the torque-speed plane, the reference current is set to maximum and the angles are set to the optimal angles of the previous point. The stored current reference is generated with the help of a PI speed controller. Thus, the correct reference value can be found at the setpoint speed for the chosen $\theta_{on}$ and $\theta_{off}$.

## 3.7 Position sensor calibration

To make sure that the position sensor outputs the correct rotor position, a calibration of the sensor needs to be done. The aim of the calibration is to find which sensor signal flank corresponds to which real angle (as specified in section 3.2). This kind of calibration needs to be done because the Hall effect sensors' physical positions might differ from the supposed ones. The sensors were found to give flanks at different positions for CW and CCW rotation, which means a calibration needs to be made for both directions. The calibration is done by placing the rotor in the aligned position and then moving it until the first flank is detected. This is done in

both directions and the two angle offsets are recorded using the testing rig's position sensor. The offset between the position sensor's first flank, in the CW and CCW directions, and the aligned position can now be used to adjust the position look-up tables, described in section 3.5.4.

## 3.8 Estimating the friction coefficient

The mechanical model of the SRM includes a friction load proportional to the machines rotational speed. To estimate the friction, a rollout test was performed where the machine was accelerated up to 3000 rpm and then released to decelerate without any external load applied. The mechanical model for the machine is described as following, where $J$ is the inertia and $b$ is the friction coefficient. Note that the inertia was estimated by drawing the rotor in CAD.

$$J\frac{d\omega}{dt} + b \cdot \omega = 0 \tag{3.8}$$

Solving the first order equation one can find the friction coefficient and mathematical model of the deceleration.

$$\omega = \omega_0 \cdot e^{-\frac{b}{J}t} \tag{3.9}$$

$$b = -ln(\frac{\omega_t}{\omega_0}) \cdot \frac{J}{t} \tag{3.10}$$

The deceleration from 3000 rpm to 500 rpm was measured and the data was filtered and processed with MATLAB to estimate the friction coefficient. See results in figure 4.5.

## 3.9 Resistance estimation

The designed resistance estimation method implements the theory described in section 2.6.1. It estimates the resistance for each phase winding which is especially useful in the sensorless flux estimation method discussed earlier in 3.5.6. The resistance has to be known at all times in order to estimate the flux linkage well. In figure 3.14, a flowchart of the method is presented. An initial resistance value is guessed, $R_0$. As long as the current for the phase is larger than 0, the current and the voltage is integrated and the flux linkage, $\lambda$, is estimated using the initial resistance value. When the current reaches 0 again, the flux linkage estimation error, $\lambda_{err}$, is calculated. The error of the resistance estimation, $e_r$, is calculated by dividing the flux linkage estimation error with the integrated current. The initial resistance's error, $R_{err,est}$, is updated by adding $e_r$ to its current value. Lastly, the estimated error is obtained by subtracting the initial resistance's error from the initial resistance value. When the phase current is greater than 0 again, the current integration and the flux linkage estimation starts over again, now using the newly estimated resistance value.

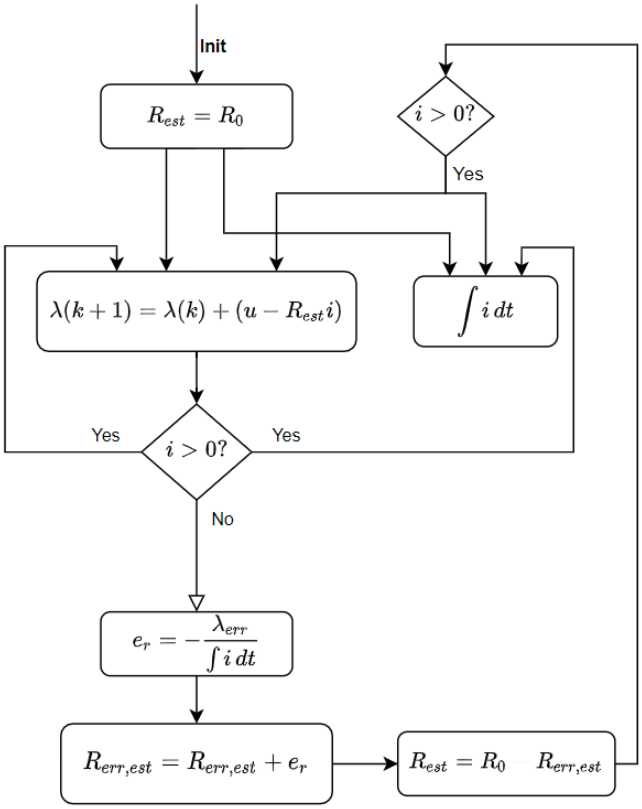


Figure 3.14: The resistance estimation algorithm.

## 3.10 Verification of LUTs in testing rig

The testing rig is a BLDC machine equipped with a torque gauge, capable of running in speed and torque control mode. The rig setup can be seen in figure 3.15. The two LUTs from the FEA, $\lambda(\theta, i)$ and $T(\theta, i)$, should be verified to see how well the simulations correspond to the machine in reality. This is done by using the methods described in section 2.3.3. In practice, a series of tests are run using the SRM in current control mode. The BLDC machine, in our tests, was set to speed control at 300 rpm. The BLDC's speed setting is a trade-off between getting good position estimation (better at high speed) for the SRM and low back-emf interference (better at low speeds). $\theta_{on}$ and $\theta_{off}$ are set to 0 and 180 degrees, respectively, for clockwise rotation and to 360 and 180 degrees for counter clockwise. These results are later spliced together to cover the entire 0 to 360 degree span. The reason why the test is divided into two sections is to be able to estimate the resistance for each current level. The tests were run by sweeping the SRM current reference in the [0.5-5] A range. For each current level, switching signals, phase currents and position were logged using ControlDesk. Torque was logged using a torque gauge that also logs angular position. This data was then used to generate the flux linkage and torque LUTs as described below.

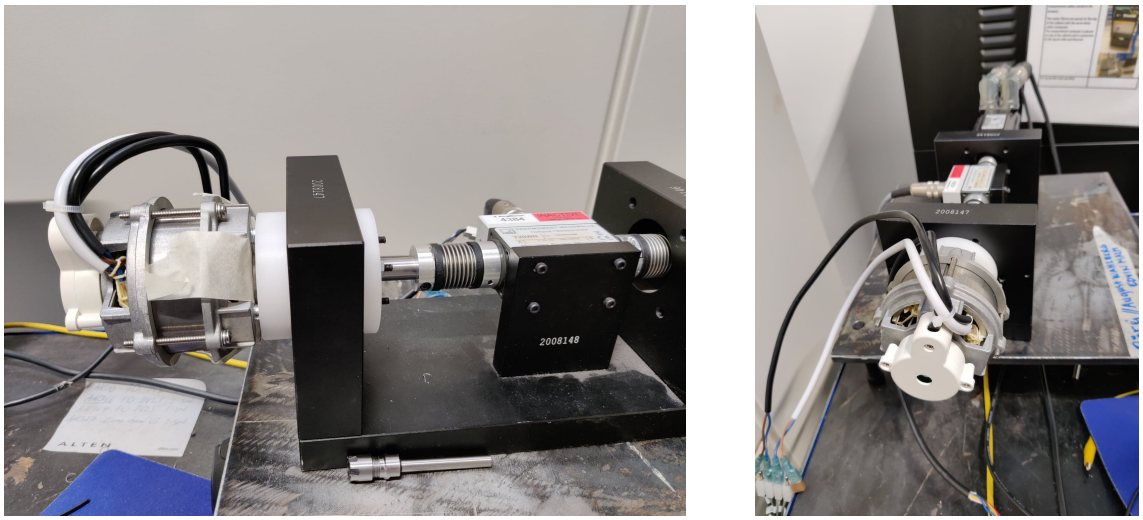

Figure 3.15: The testing rig setup. From the left side: SRM, torque gauge and BLDC machine.

### 3.10.1 Generating the flux linkage LUT

The flux linkage, for a given current level, is obtained using the method described in section 2.3.3. Equation 2.6 can be represented in discrete form as follows:

$$\lambda_{ph}(k+1) = \lambda_{ph}(k) + (u_{ph} - R \cdot i_{ph})T_s \tag{3.11}$$

For each current level, the period where the current is active is extracted from the logged data, see figure 3.16. This period is longer than $\theta_{on}$ to $\theta_{off}$ since the current needs some time to reach 0 after the current reference has been set to 0. For the period, the flux linkage is calculated using the integration method. The phase voltage level is logged on beforehand for each current level and is thus used in the integration. However, in the performed measurements the flux linkage did not return to 0 at the end of the excitation period. For low currents, the phase voltage was too high and for high currents, the phase voltage was too low. To fix this, resistance values were determined for each current level by trying various values until the calculated flux linkage reached zero by the end of the period (see section 2.6.1 about resistance estimation). This method of varying the resistance is not theoretically correct, considering the resistance needed to be changed between 1.8→0.95 Ω for currents between 0.5→5 A. Copper's temperature coefficient is 0.039 which means it will change its resistance about 0.4% per degree Kelvin. The temperature most likely didn't change enough to explain this difference. Instead, this approach can be considered a practical way of acquiring a good approximation of the result, even with measurement errors. The reason the voltage didn't integrate in the expected way was likely due to some sort of measurement error, either in the voltage or current measurement. A small measurement error integrated over a long time leads to a large error in the end but can be corrected by varying another parameter, in this case the resistance. The flux linkage was averaged for n=15 periods to better account for noisy measurement data. The data is plotted in the results chapter, figure 4.8a.

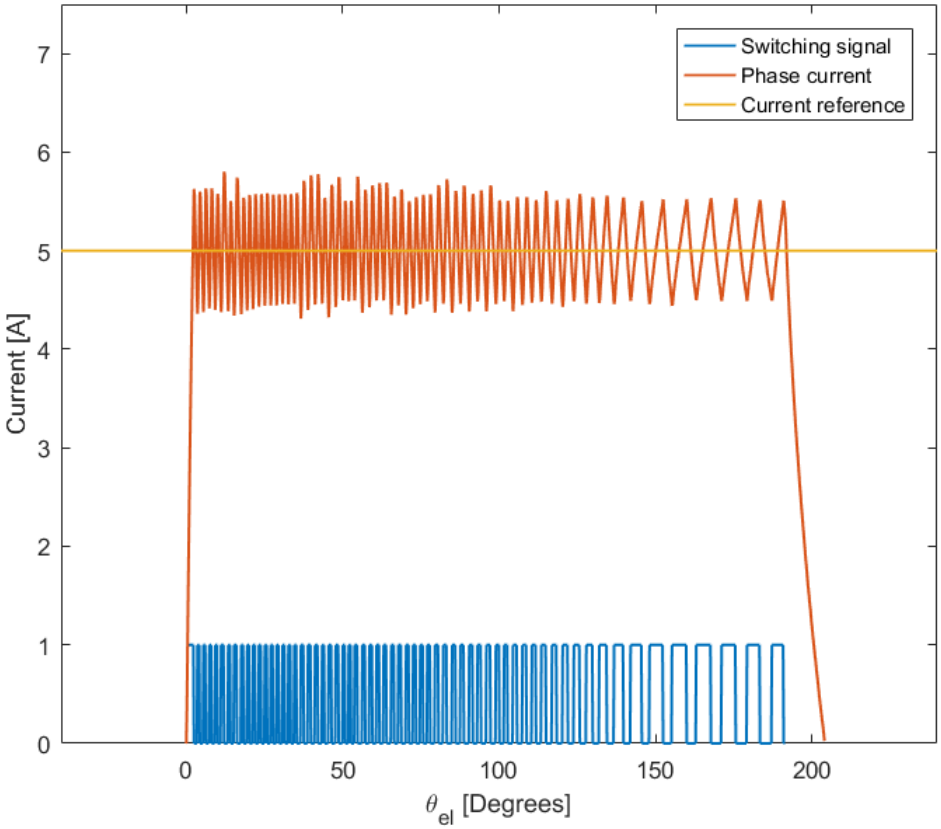


Figure 3.16: Example of a current period, where the current is greater than 0. $i_{ref} = 5$ A, $\theta_{on} = 0°$, $\theta_{off} = 180°$.

### 3.10.2 Generating the torque LUT

In order to be able to utilize the logged torque data, the angle offset between the torque gauge and the SRM's axis needed to be found. This was done by placing the rotor at a known angle, in this case the "locked" position (the angle where the air gap between rotor and phase is minimal, the reluctance is the lowest and no torque is produced). The rotor was then moved until the SRM registered a position flank. The offset between the "locked" position and the first hall sensor flank for the SRM had been found earlier. This enabled the offset between the torque gauge and the SRM to be found by observing the torque gauge's initial and final positions. The torque from the torque gauge logging could then be plotted in the SRM's coordinate system, using the more precise position data from the torque gauge. Before being plotted, the torque data was post-processed. The friction in the rotational direction was determined and added to the measured data from the torque sensor. This was necessary to get the actual produced torque from the SRM. The friction (resistance in testing rig) was determined by logging the output torque at the set speed, 300 rpm, with the SRM's current turned off (also accounting for the calibration error). Then, an average was taken over n=10 periods of torque data for each current level to better account for measurement noise. The data was then filtered using a moving average filter to minimize noise but still keep the measure characteristics. The result is plotted in the results chapter, figure 4.7.

## 3.11 Validation of measured LUTs

To see how well the measured LUTs represents the real machine, the LUTs were implemented in the ITC and ATC controller. Tests were performed in the rig using both the simulated and measured LUTs to evaluate which is most accurate to the real machine. The test runs consist of finding the maximum load torque where the SRM can keep a certain speed. Tests were run at 500, 1500, 2500 rpm and max speed for CW and CCW direction. This data was later used to generate torque-speed curves for the different LUTs used. The idea is to use the torque-speed curves to be able to compare how well the measured and simulated LUTs represent the real machine. The assumption is that the most accurate LUTs will result in the best performance. The results from these tests are presented in figure 4.18 in the results chapter and analysed in the discussion.

## 3.12 Validation of Simulink/machine model

To see how well the Simulink model represents the real machine, tests were run with the same conditions in both Simulink and on the testing rig. The same tests as described in 3.11 were used to generate torque-speed curves from Simulink and experimental runs, using both measured and simulated LUTs. To validate the Simulink model the assumption is made that an accurate Simulink model will result in similar torque-speed curves for the tests run in Simulink and on the testing rig.
Tests were also made where the machine was loaded with a torque; 0, 1.5, 3 and 4.5 Ncm, and the output torque reference setpoint was logged. Another assumption was that if the machine model is a perfect representation of the real machine, the torque reference will equal the torque load plus the friction torque in both Simulink and testing rig runs. If there is a difference in the results this means that there is a difference in the machine model compared to the real machine. This error can be either in the friction model or the LUTs, or a combination of both. The results from these tests are presented and analysed in section 4.5.2.

## 3.13 Evaluation of controllers in testing rig

To compare the control methods, ITC and ATC, tests were performed in the testing rig to observe the highest loads at which the SRM can keep a certain reference speed, for a range of speeds. The speeds tested were 500, 1500, 2500 rpm and the maximum speed at no load. The idea is to compare how well the two control methods (ITC and ATC) perform over the speed range. Torque-speed curves were obtained from the tests and the result can be seen in section 4.5.3. To get a deeper understanding for how well the performance of the two control methods differ, tests were also performed where the speed ripple of the SRM was logged. This is especially important in BorgWarner's oil pump application since a speed ripple variation in the actuator (and not the actual torque ripple) is what results in a torque variation in the clutch in the end. See results in sections 4.20 and 4.21.

# Chapter 4

# Results and Discussion

## 4.1 Simulated and Inverted Look-Up Tables using FEA

Figures 4.1 and 4.2 are the results of the FEA performed to create the machine model. The simulated look-up tables $\lambda(\theta, I)$ and $T(\theta, I)$ are inverted to the desired relations $I(\theta, \lambda)$ and $I(\theta, T)$. The graphs show the machine characteristics from a symmetric machine model figure 4.1, and asymmetric machine model figure 4.2. Note that the rotor position 0° is defined as unaligned and that 180° is when the rotor is symmetrically aligned with the active stator pole. See 3.2 for a more detailed explanation of the definition of rotor position.

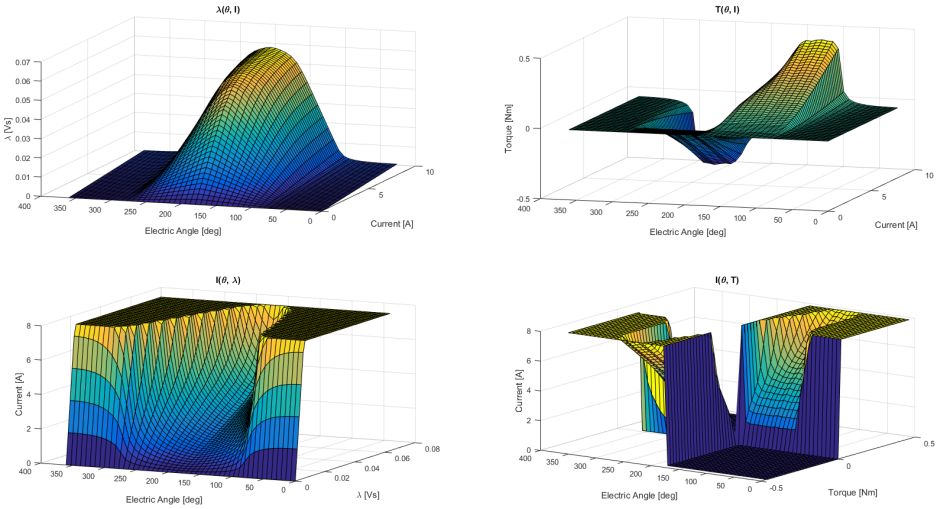


Figure 4.1: Symmetric machine characteristics.

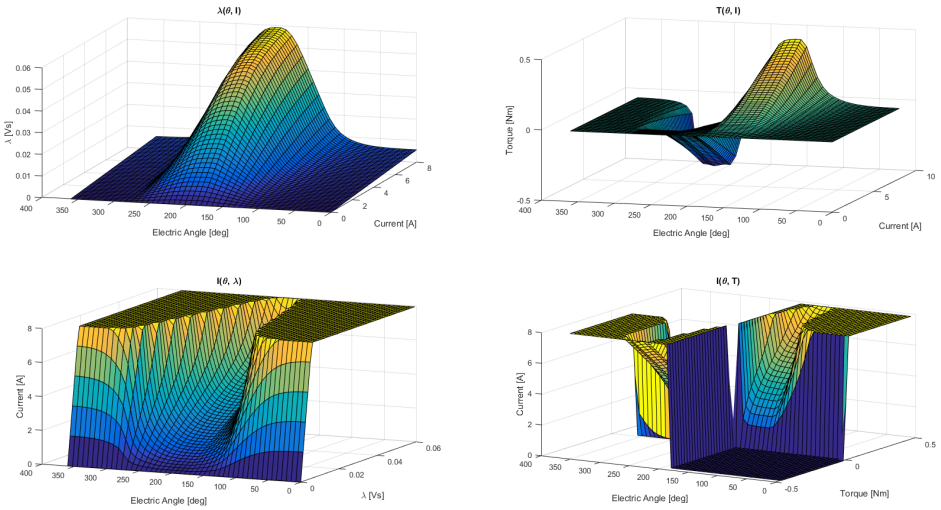


Figure 4.2: Asymmetric machine characteristics.

The simulated LUTs show typical characteristics of an SRM. One can see that $\lambda(\theta, I)$ and $T(\theta, I)$ have a nonlinear relationship and that the machine is weak close to its unaligned position. The symmetric machine model, figure 4.1, can be seen to have zero torque at its aligned position while the asymmetric model, figure 4.2, has a positional offset in where zero torque is produced.

### 4.1.1 Speed compensation of simulated LUTs

Figures 4.3 and 4.4 show the simulated LUTs which has been speed compensated according to 2.5.1. It is clear how at higher speeds (more back emf) the turn on angle is decreased to give the current enough time to rise to reach its reference at the start of the electrical stroke.

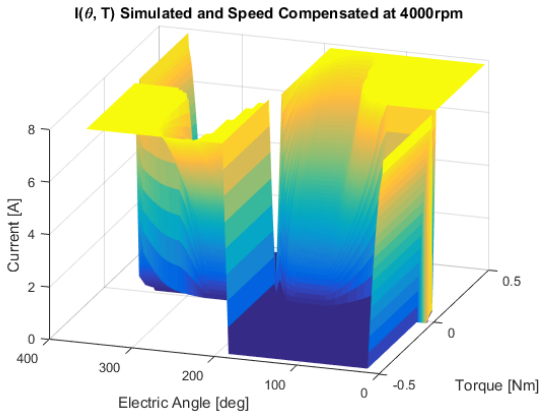


Figure 4.3: The speed compensated inverted torque LUT at 4000 rpm.

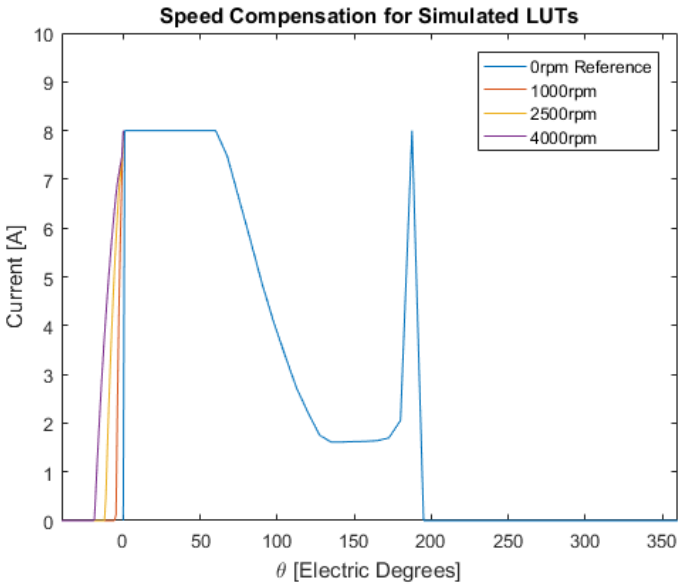


Figure 4.4: A slice of the speed compensated inverted torque LUT is shown at $T = 2.4$ Ncm at 3 different speeds along with the uncompensated at 0 rpm.

## 4.2 Measurement of Friction

To generate a Simulink machine model that accurately corresponds to the real machine, the friction is estimated both for the machine itself and when it is connected to the testing rig. Figure 4.5 shows data acquired from a rollout test which is used to calculate the mechanical friction coefficient of the machine itself. The frictional coefficient is calculated using 3.10.

$$b = -ln(\frac{\omega_t}{\omega_0}) \cdot \frac{J}{t} = -ln(\frac{500}{3000}) \cdot \frac{2.7 \cdot 10^{-5} kgm^2}{1.78s} = 2.72 \cdot 10^{-5} Nms \tag{4.1}$$

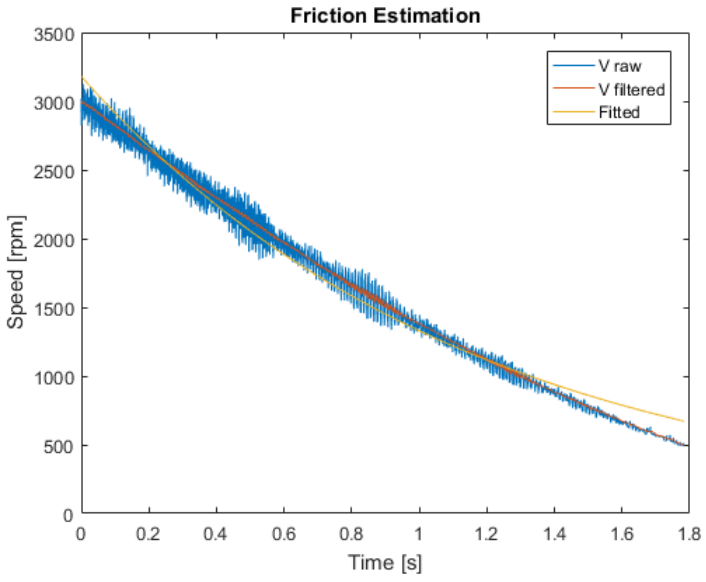


Figure 4.5: Deceleration from 3000 rpm to 500 rpm with no external load.

A similar rollout test was also done in the testing rig, see figure 4.6. The frictional coefficient is calculated using 3.10. Note that the same inertia, as for the machine itself, is used for the calculations of the machine in the testing rig. This simplification is done since most of the inertia is estimated to be in the SRM rotor.

$$b = -ln(\frac{\omega_t}{\omega_0}) \cdot \frac{J}{t} = -ln(\frac{500}{4000}) \cdot \frac{2.7 \cdot 10^{-5} kgm^2}{0.67s} = 8.35 \cdot 10^{-5} Nms \tag{4.2}$$

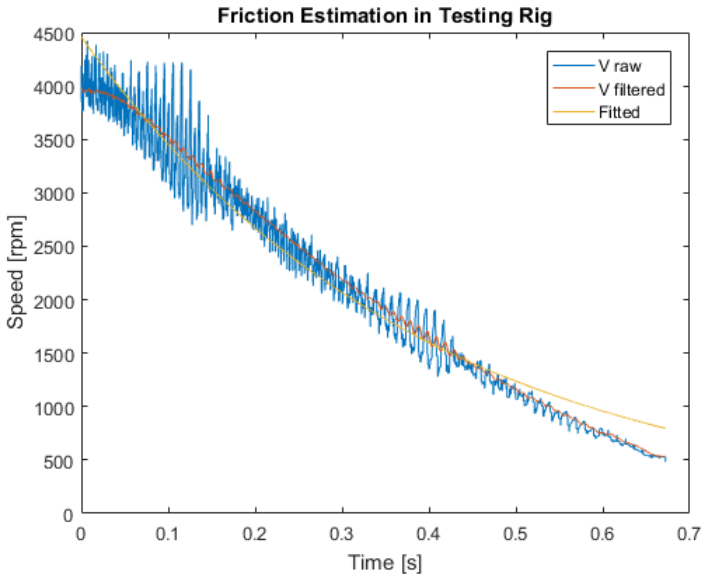


Figure 4.6: Deceleration from 4000 rpm to 500 rpm with no external load in testing rig.

The braking BLDC machine was run without the SRM producing torque to measure the braking load in the testing rig. Figure 4.7 shows the average frictional load measured during 7 full rotations in the testing rig at 300 rpm. This data is later taken into consideration when the measurements of the produced torque of the SRM are analyzed to generate the measured look-up tables.

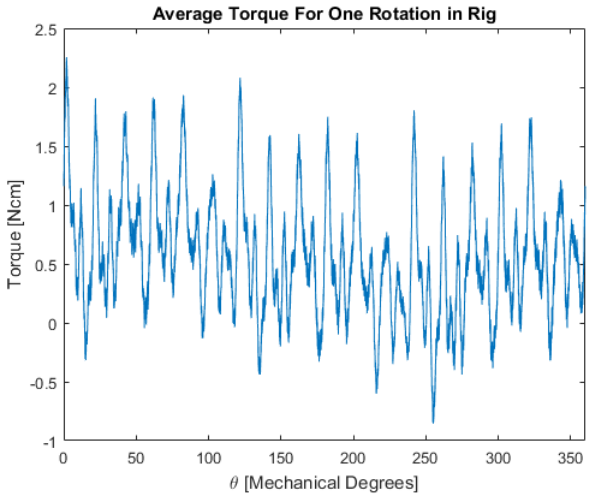


Figure 4.7: Average of measured torque during a full mechanical rotation in the testing rig.

## 4.3 Verification of lookup-tables

### 4.3.1 The flux linkage LUT

Data, obtained from the method described in section 3.10.1, is put together to form the flux linkage LUT seen in figure 4.8a. It is then filtered in order to get rid of the noisy measurements, the result can be seen in figure 4.8b.

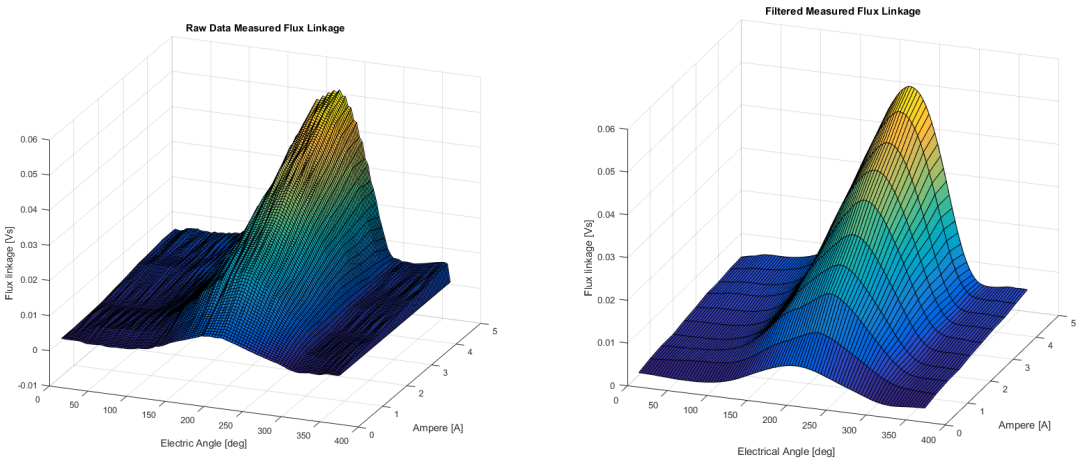


(a) Raw data measured flux linkage LUT (b) Filtered measured flux linkage LUT

Figure 4.8: Flux linkage before and after filtering.

### 4.3.2 Measured flux linkage LUT comparison with simulations

To be able to more easily compare the measured and simulated flux linkage LUTs with each other, the surfaces were projected in the $\theta$-$\lambda$ plane and can bee seen in figure 4.9. The different lines represent a certain current level, from 0.5 A (blue) to 5 A (red).

Overall, the simulated and measured values are similar, they have roughly the same peak heights and shape for each current level. One aspect where they differ, however, is at what electrical degree the peak is. The simulated curve's peak is at about 187.5° while the measured curve's peak is at about 211°. There are several possible reasons for this discrepancy. The FEA could have been slightly off due to inaccuracies in measuring the machine's geometry and due to insufficient material data. Another reason for the difference could be that the offset between aligned position and the Hall sensor's position was measured inaccurately. If the offset between the position sensor and the machine's coordinate system was measured incorrectly, the peak of the flux linkage LUT would shift with the offset error. This error is, however, thought to be significantly smaller than the angle difference shown in the plots. The reason being that the torque LUT shows the same characteristics (peak at 205°) and its position was measured independently to the SRM's (using the torque gauge's position sensor).

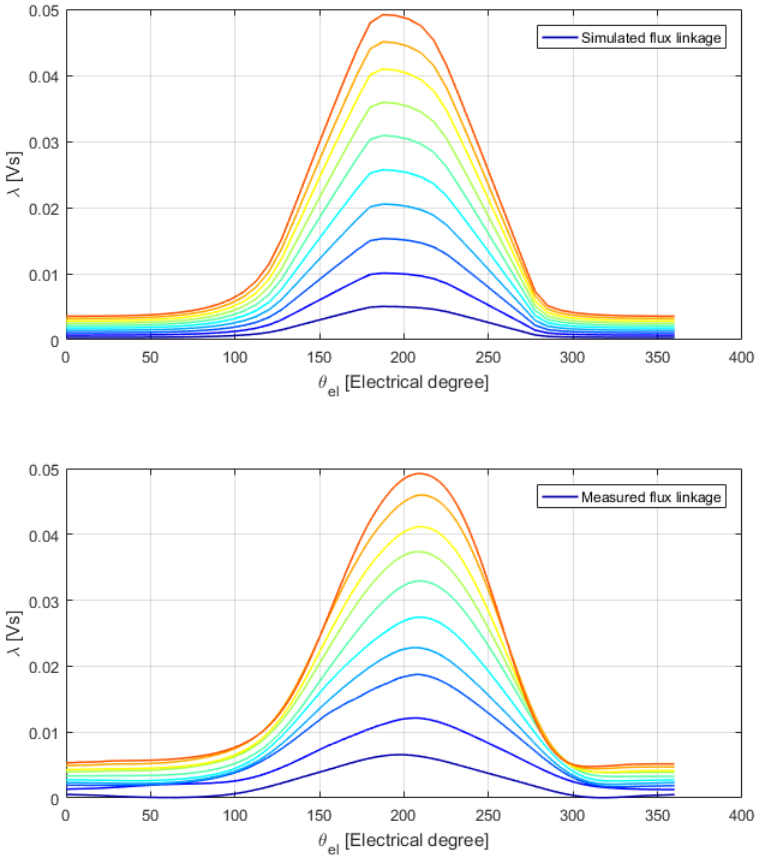


Figure 4.9: Simulated vs measured flux linkage for 0.5 A (blue) to 5 A (red).

### 4.3.3 Measured torque LUT generation

The produced torque of the SRM was measured according to 3.10.2 at current levels between 0.5 and 5A. The torque produced by the machine was measured during a full electric stroke while the current was held constant. The measured $T(\theta, I)$ can be seen in figure 4.10a. The measurement data is filtered with a moving average and calibrated using the measured frictional load shown in 4.7, the resulting LUT is shown in 4.10b.

### 4.3.4 Measured torque LUT comparison with simulations

To compare the simulated and the measured torque LUTs, a 2D plot is generated for a full electric stroke, see 4.11. One can see how the torque region is narrower for the simulated LUTs and that there is an offset between where the "locked" position is (at maximum inductance). As discussed in the comparison between measured and simulated flux LUTs, these discrepancies can be explained by poor geometrical measurements of the rotor for the simulated LUTs. The "locked" position of the rotor, at 205°, is also confirmed from the position sensor calibration. This confirms the validity of the measurements. Also note that the characteristics of the simulated and measured LUTs are similar. One can also observe the asymmetry in both the

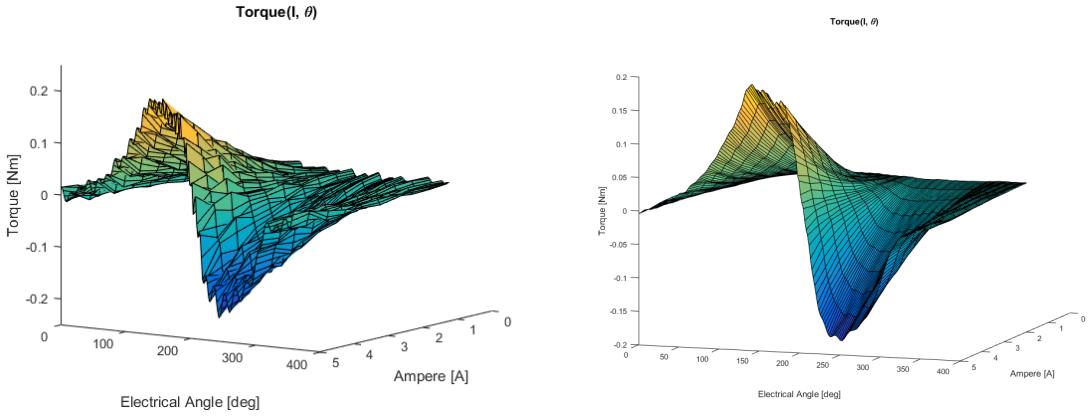


(a) Raw (b) Filtered

Figure 4.10: Measured torque look-up tables.

simulated and measured LUTs. In both cases an aligned rotor (180°) would produce a positive torque.

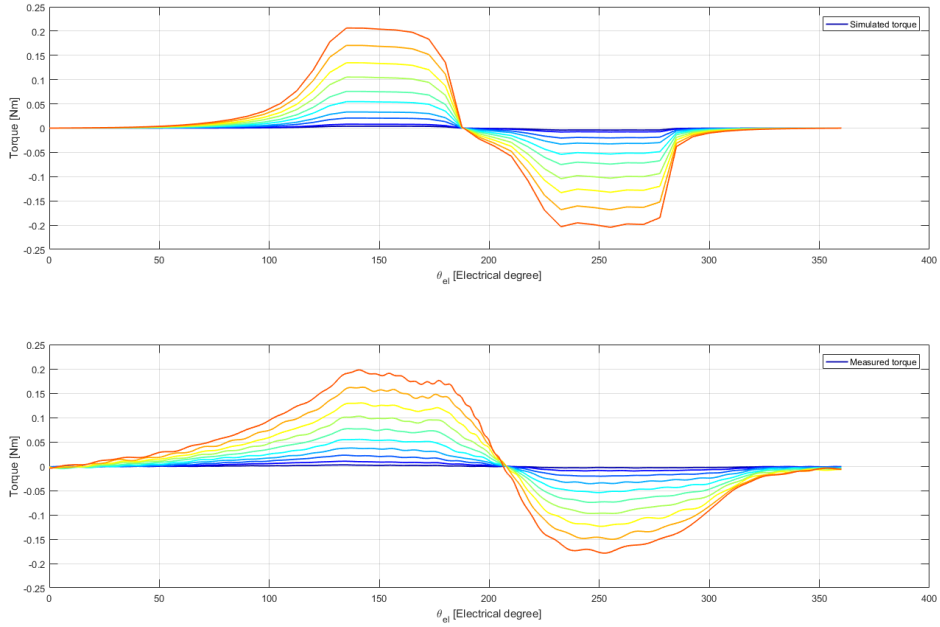


Figure 4.11: Torque generation with simulated LUTs compared with measured LUTs during a full electric stroke.

### 4.3.5 Measured and filtered LUTs with Inversions

The measured LUTs $\lambda(\theta, I)$ and $T(\theta, I)$ are inverted so that they can be used in the ITC current controller. Figure 4.12 shows the filtered LUTs with their corresponding inversions $I(\theta, \lambda)$ and $I(\theta, T)$.

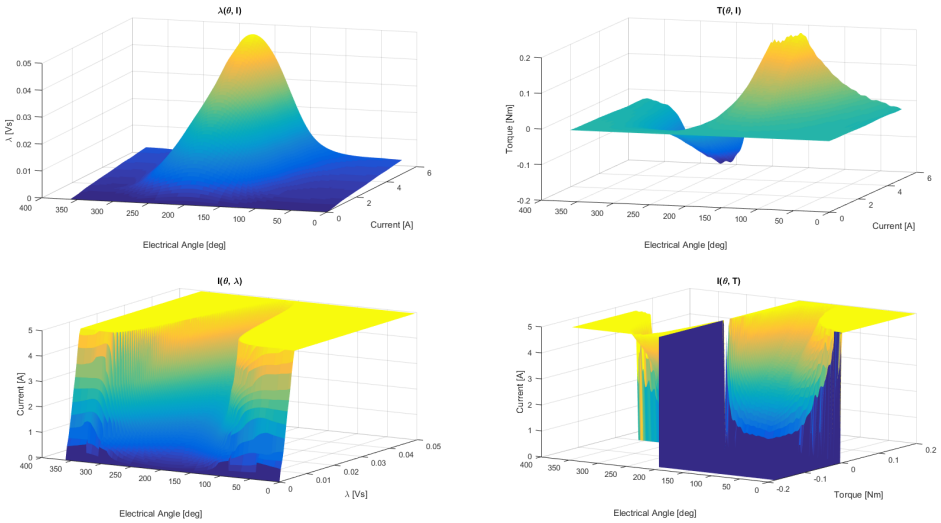


Figure 4.12: Measured machine model characteristics.

### 4.3.6 Speed compensation of measured LUTs

Speed Compensation is also performed for the measured LUTs. The results are similar to the speed compensated simulated LUTs and can be seen in figure 4.13 and 4.14.

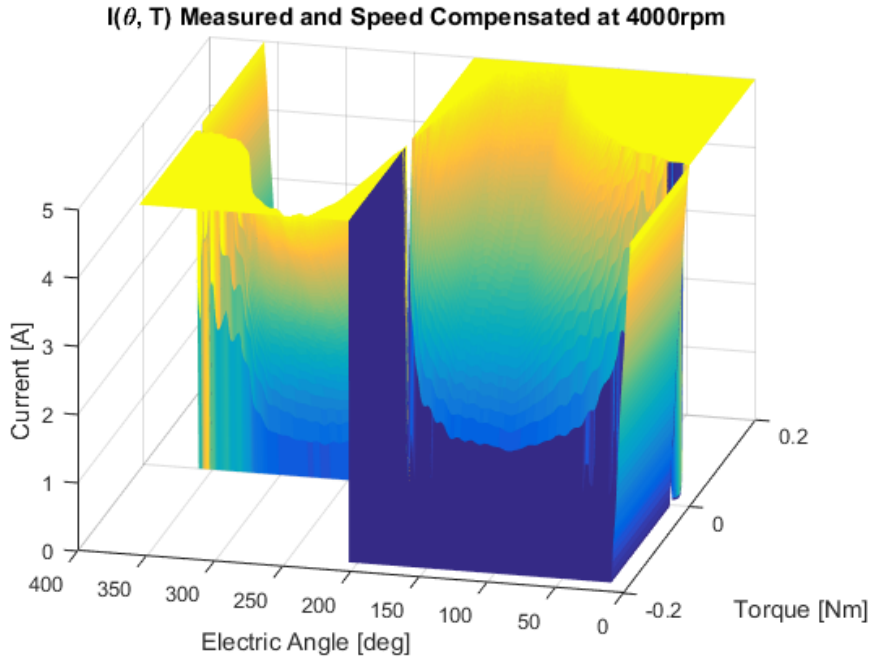


Figure 4.13: The speed compensated inverted torque LUT at 4000 rpm.

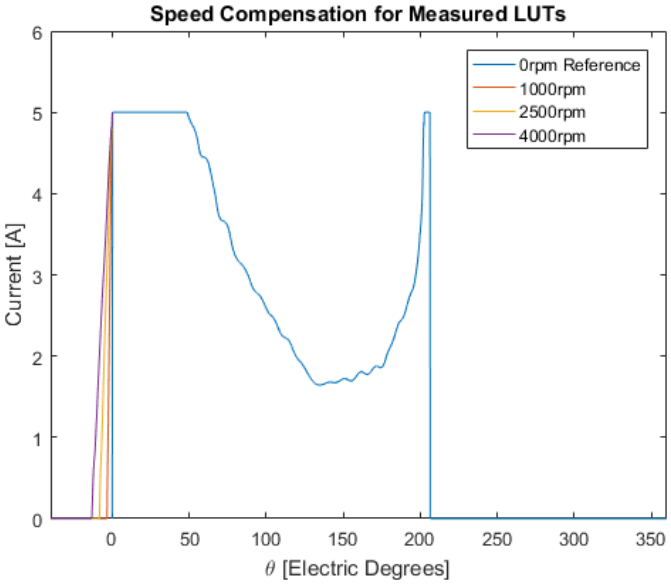


Figure 4.14: A slice of the speed compensated inverted torque LUT is shown at $T = 2.4$ Ncm at 3 different speeds along with the uncompensated at 0 rpm.

## 4.4 ATC Optimization

The following figures show the results of the ATC optimization both with the simulated LUTs and the measured LUTs. The figures show the optimal control variables at different operating points where minimized speed ripple and copper losses are weighed at 80% and 20% respectively. Since speed ripple is the most important performance factor it was set to 80%. This resulted in control variables that minimized the speed ripple sufficiently but did not keep a current on during inefficient parts of the electric stroke.

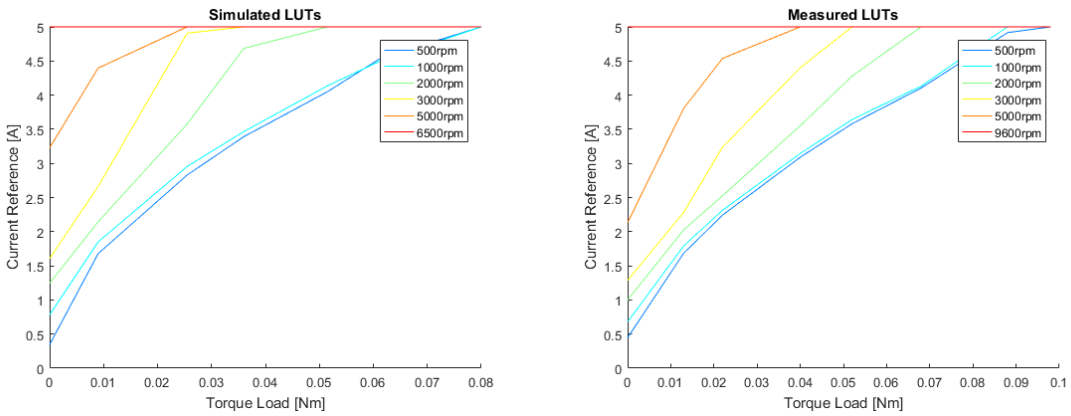


(a) Simulated LUTs (b) Measured LUTs

Figure 4.15: Optimal Current references for ATC.

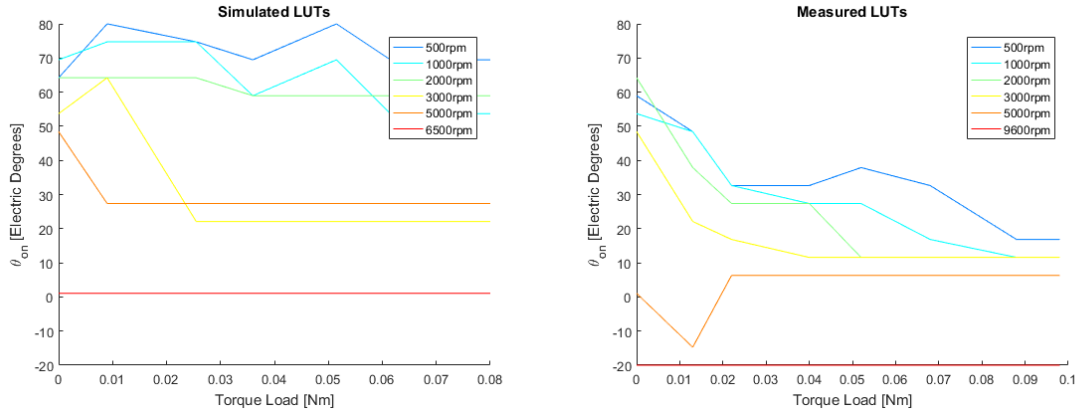


(a) Simulated LUTs (b) Measured LUTs

Figure 4.16: Optimal $\theta_{on}$ references for ATC.

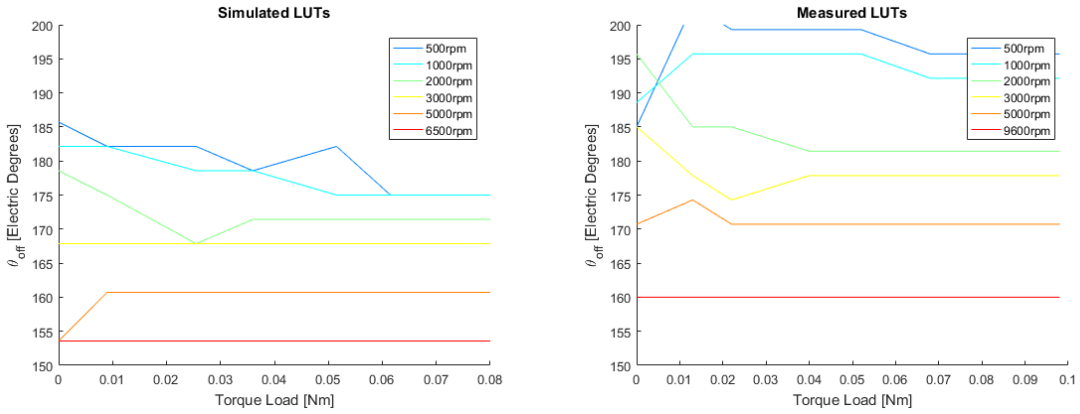


(a) Simulated LUTs (b) Measured LUTs

Figure 4.17: Optimal $\theta_{off}$ references for ATC.

The results show that the current references are increasing as the load torque and speed is increasing. This is expected since a higher current will generate more torque which is necessary at both higher loads and higher speeds due to friction. Note that for the measured LUTs the required current reference is somewhat lower than the simulated. This can be explained by figure 4.11 which shows that there is a broader part of the electric stroke where it is possible to generate torque in reality. Therefore, the same conduction period with a lower current can produce equal amount of average torque.

The turn on angles shown in figures 4.16a and 4.16b both show that at higher speeds the turn on angle is decreasing. This is due to a higher back emf at high speeds which results in a lower turn on angle of the phase to reach the reference current on time. A relationship where the turn on angle decreases with increasing load can also be seen for the optimization with the measured LUTs. Since the measured LUTs can generate torque earlier in the stroke the copper losses can be minimized with a lower current for a longer part of the electric stroke. This relation is not found in the optimization with simulated LUTs which have almost no torque production

available between 0 and 80 electrical degrees as shown in figure 4.11.

The turn off angle, similarly to the turn on angle, is decreasing with higher speeds. Since the current should fall to zero before the negative torque generation region is entered, the turn off angle is decreased to allow enough time for the current to fall. Note the offset between the turn off angles between the simulated LUT and measured LUT optimization which is due to the offset in the locked position of the different LUTs, discussed in previous sections.

## 4.5 Performance and Evaluation of controllers in Testing rig

### 4.5.1 Validation of measured LUTs

The measured look-up tables were incorporated into the ITC and ATC controllers and tests were carried out as described in section 3.11. This results in two torque-speed curves, seen in figure 4.18. As described earlier, the idea is that the control method with the best representation of the machine would perform the best. From the results it is apparent that the measured LUTs perform better for both ITC and ATC than the simulated/FEA ones. This shows that it is likely that the measured LUTs represent the real machine better than the FEA LUTs. The reason why the FEA is inaccurate is probably due to errors in measuring the SRM's geometry. Especially the rotor geometry was difficult to get right since it is encapsulated in hard plastic. Had the geometry been measured with greater precision it is likely that the control using the simulated LUTs would perform at least as good as the measured LUTs.

The difficulty in the measurement method lies in getting accurate measurements of positions (offsets etc.) and in finding ways to minimize noise in sensor measurements. The difficulty with the FEA method is rather how to know how reliable the results are. Both of the discussed methods have their pros and cons and we believe they complement each other in a good way. For us, the FEA LUTs were useful to have in the early stages of developing in order to design a working controller. The measured LUTs were useful because it was unknown how well the FEA was made. If the FEA is made with greater precision (in another project perhaps), it could be superfluous to measure the LUTs. An FEA that is well made captures all the machine dynamics and could be used throughout the whole project.

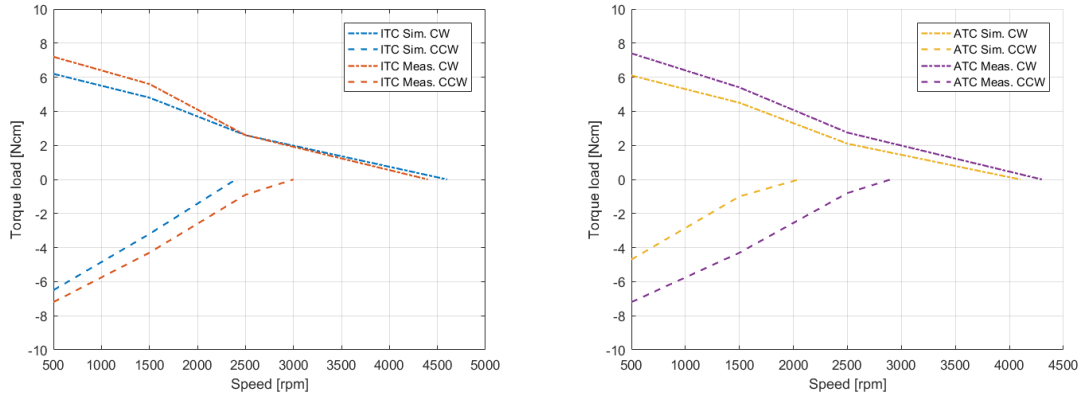


(a) Comparison of ITC methods (b) Comparison of ATC methods

Figure 4.18: Torque-speed curve for the two control methods in testing rig with measured and simulated LUTs.

### 4.5.2 Validation of Simulink Model

As explained in 3.12, both Simulink simulations and testing rig runs are performed with the measured LUTs. Figure 4.19 shows the highest possible load at which the machine can run for the different control methods.

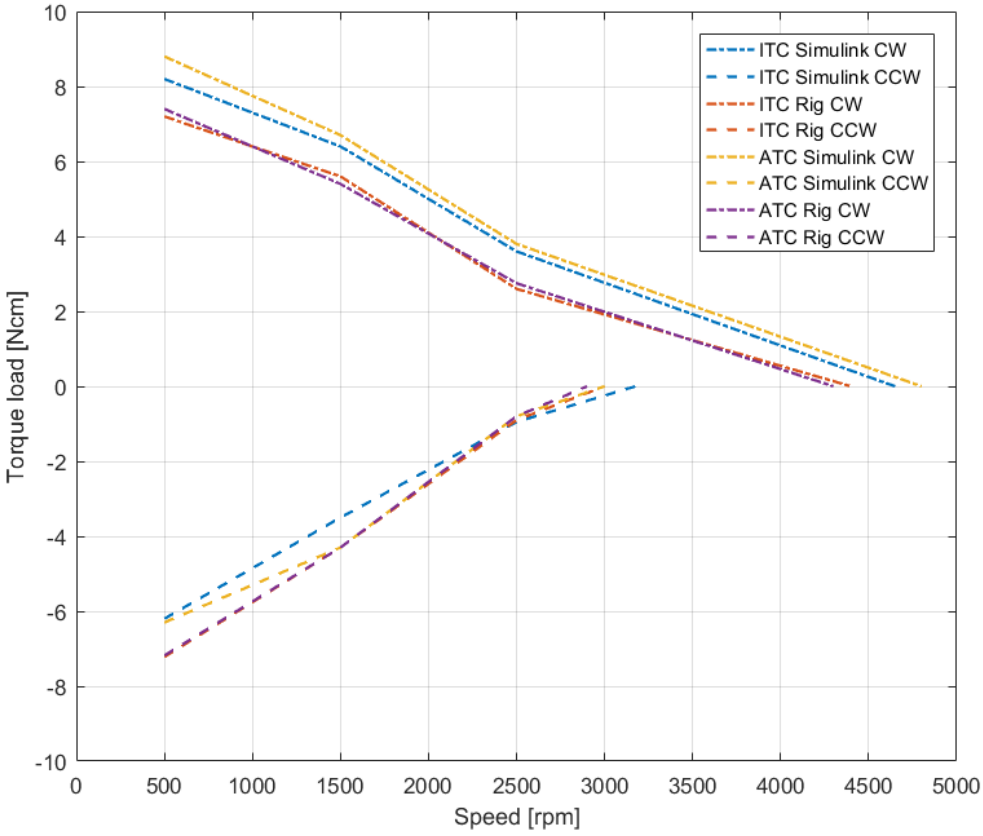


Figure 4.19: Torque-speed curves in Simulink and testing rig compared for the two control methods, using measured LUTs.

The machine was also run using the measured LUTs at the following operating points where the torque reference setpoint was noted. See table 4.1 and table 4.2.

| ITC Measured CW Simulink | | | |
|---|---|---|---|
| Load [Ncm] \ Speed [rpm] | 500 | 1500 | 2500 |
| 0 | 0.4 | 1.3 | 2.4 |
| 1.5 | 2.0 | 3.2 | 4.7 |
| 3 | 4.0 | 5.4 | 8.5 |
| 4.5 | 6.5 | 8.2 | - |

Table 4.1: Torque References setpoint required at the different operating points in Simulink.

| ITC Measured CW Testing Rig | | | |
|---|---|---|---|
| Load [Ncm] \ Speed [rpm] | 500 | 1500 | 2500 |
| **0** | 2.5 | 3.5 | 5.1 |
| **1.5** | 4.8 | 5.7 | 7.3 |
| **3** | 7.5 | 8.7 | - |
| **4.5** | 10.8 | 12.5 | - |

Table 4.2: Torque References setpoint required at the different operating points in Testing Rig.

It can be seen from figure 4.19 that the performance in the Simulink simulations is considerably better than in the testing rig for CW rotation. This is true for both control methods. In CCW, however, the rig tests surprisingly outperformed the Simulink simulations. It is surprising since the simulations use the exact same machine model for simulating the machine and for the control of it. In the rig there is likely some sort of discrepancy between the actual machine and the machine model that is used for controlling it and so the performance should be worse. This suggests that there is a discrepancy between the Simulink model and the machine running in the testing rig. Since the Simulink machine model and its control method is based on the measured LUTs, which in turn have been measured in the same testing rig, the LUTs should be an adequate representation of the machine dynamics. This is also supported by the fact that the FEA simulations and the measured LUTs are considerably similar.

An explanation for the differences in performance could be an insufficient model of the friction in the testing rig. Even though a friction coefficient is estimated in the testing rig and used in the simulations, the proportionality between frictional load and speed is heavily simplified. The resistance in the rig is, as can be seen in figure 4.7 at 300 rpm, oscillating during a full rotation. This suggests that the resistance in the rig is not constant at a certain speed which corresponds to load disturbances

not taken into regard in simulations.

By analyzing tables 4.1 and 4.2, the difference between torque reference setpoints and the applied load can be seen for both the simulation and in the testing rig. The Simulink simulation results show that for higher loads, the differences between the torque reference setpoint and load increases. Since there is no unaccounted-for friction in the Simulink model the increasing difference cannot be motivated by frictional load. A possible explanation could be the increasing speed ripple at the higher loads, because of the torque ripple of a 4/2 SRM. A higher speed ripple would require the machine to accelerate more and thus need a higher torque setpoint.

### 4.5.3 Performance of control methods

#### Torque-speed curve

From the tests performed in the testing rig, described in section 3.13, the torque-speed curves seen in figure 4.20 can be generated. It can be seen that in the CW direction, ITC and ATC using the measured LUTs have very similar performance. In the CCW direction, however, the control methods with simulated LUTs perform significantly worse than the measured ones. Noticeably, the ATC performs the worst which is reasonable since it has optimized its commutation angles to match a machine which has a wider electric stroke in CCW than in reality. Thus, it incorrectly keeps the current on for a longer period, producing negative torque on the real machine, resulting in worse performance.

The ITC, in CCW, with simulated LUTs also perform worse than with the measured LUTs. Similarly to the ATC, the required current reference to produce a stable torque is incorrectly simulated. Thus, it is expected that it does not perform as well as with the measured LUTs.

Another result that is worth mentioning is that ITC with simulated LUTs surprisingly outperform the other control methods in CW in means of no load speed (max speed). This is most likely due to its turn off angle being chosen in regard to the simulated LUTs. For ITC, the turn off angle is chosen as 15 electrical degrees before the torque reaches 0 in the torque LUT. In the simulated LUTs case that results in a turn off angle about 20° smaller compared to the measured LUTs case. Therefore, ITC with simulated LUTs turns off its current in time for it to reach zero without producing negative torque for higher speed, where the current has less time to fall. As mentioned, both ITC methods use a constant turn off angle chosen in regard to the electrical stroke of the LUTs. A lower turn off angle might be favorable for the ITC with simulated LUTs at max speed.

A reason to why the ITC with simulated LUTs can possibly outperform the ATC, in regard to maximum speed, with measured LUTs is due to the setup of the ATC optimizations. The ATC is optimized on a model that does not have an accurate model of the friction in the testing rig. It could have found control variables, for a certain operating point, that do not perform adequately in reality and thus causing it to lack in performance. Also note that at maximum load, the current references for ITC and ATC are very similar since maximum torque is required throughout the

electric stroke. Therefore, the ITC would have a similar current profile as the ATC at maximum no load speed. Thus, the only parameter which can cause the ITC with simulated LUTs to outperform the ATC would be the turn off angle, being favorable for the ITC with simulated LUTs.

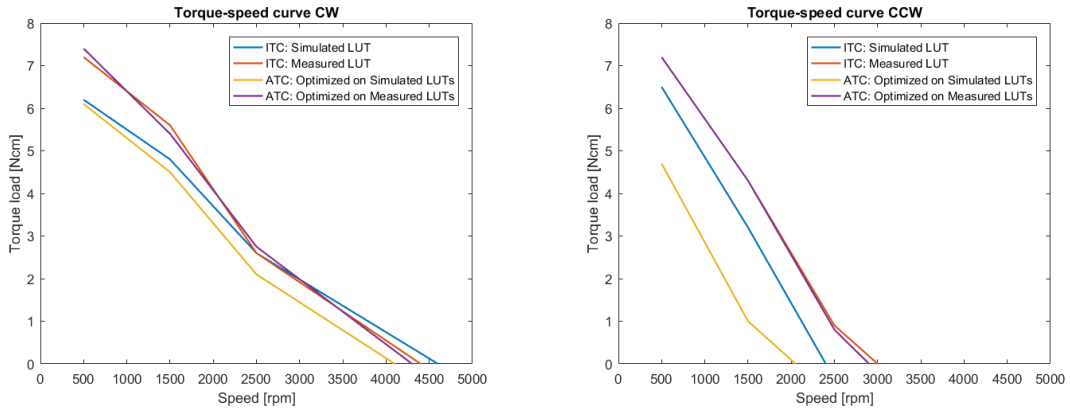


(a) Comparison of control methods for CW rotation

(b) Comparison of control methods for CCW rotation

Figure 4.20: Performance of control methods comparison.

### Speed ripple

From the testing rig runs that are used when validating the Simulink model, speed ripple is calculated. The speed ripple is calculated using equation 3.5, calculating the RMS value relative to the mean value of the measurement. The maximum speed is not included, however, since it is different for each control method. Only testing points where a steady speed could be kept were included. The results below, in figure 4.21, are for ATC and ITC respectively with measured LUTs in CW direction. It can be observed that ATC performs slightly better than the ITC at higher speeds (1500 and 2500 rpm). As mentioned before, this is thought to be due to non-optimized turn off angles for the ITC. The current, again, decreases more quickly at higher speeds (because of higher back emf, see equation 2.7) but has less time to do so (because of the higher speed). It is noticed that for high speeds, the current does not have time to come down to 0 before the rotor passes into the negative torque region. This means that the current keeps producing negative torque in a region where not much positive torque can be produced (by the other phase). The result of this is a higher torque ripple and consequently a higher speed ripple, than in optimal conditions. It is believed that optimizing the theta off angle for the achievable speed range would give the ITC a result better than the ATC. This is because in theory, ITC can deliver a smoother torque than ATC can because of the difference in the shape of their current profiles.

In a test in the testing rig with the existing BLDC actuator run at ∼1200 rpm, 3.5 Ncm load and no pump connected, the speed ripple was below 1%. As a comparison, the 4/2 SRM is at best 4% (at 500 rpm) and at worst 9% (at 1500 rpm). It seems like the inherent high torque ripple of the 4/2 SRM gives relatively high speed ripple

as well, even though efforts have been made to reduce it.

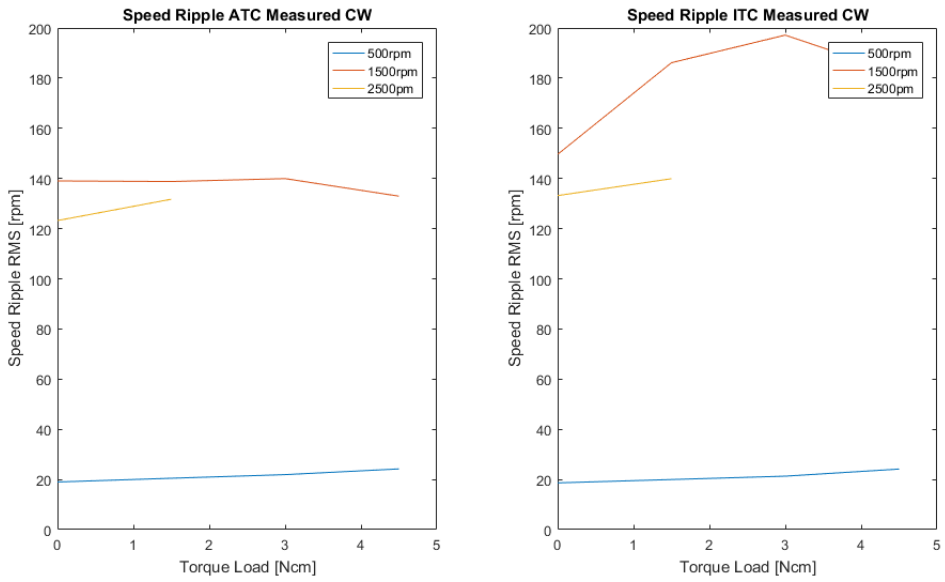


Figure 4.21: ATC and ITC speed ripple (measured LUTs).

## 4.6 Sensorless position estimation

The following results are from simulation testing of the sensorless position estimation, presented in section 3.5.2. Tests were performed to evaluate the start-up sequence and the sensorless position estimation.

The start-up sequence had problems working in simulations but worked well on the physical machine. It seemed like the machine has more torque close to the "locked position" when exciting the other phase than is captured in simulations. This caused the rotor to be unable to move from the "locked position" in simulations, even though it moved as expected in the real machine. Additional problems were encountered when the machine was put into the testing rig. The testing rig has substantially more friction ($\sim$ 3 times) than the free-standing machine. This caused the start-up sequence to fail since the rotor wouldn't accelerate at the expected rate. This is a big drawback with this method of blindly turning on currents in a pre-decided pattern. Because the sequence is designed for one load case scenario, it behaves poorly when the circumstances changed. An improvement of the algorithm would need to be implemented in order to accommodate different load scenarios.

For a machine with higher number of phases, an idea could be to use the self-inductance method at low speeds where it works well and then at higher speeds switch over to another method like the flux-based estimation implemented here. For a 4/2 SRM, however, the self-inductance method would probably perform poorly. The inductance of the machine has the same form as the flux linkage seen in figure 4.9. One can see that the derivatives of the lines are close to 0 from about

0° to 80° and from about 300° to 360°. As mentioned in the theory section, the self-inductance method relies on change in inductance to work. Where there is close to no change, it would perform poorly. This poses a big challenge for sensorless position estimation of the 4/2 SRM since most of the estimation methods suitable for low speeds use inductance based estimation. One method that goes around this problem is the "Inductance inflection point", presented by R.Kim and J.Kim in [17].

In the following results, figures 4.22, 4.23 and 4.24, the SRM is controlled using the real rotor position and speed. The flux linkage estimation was run in the background to evaluate its performance in optimal conditions.

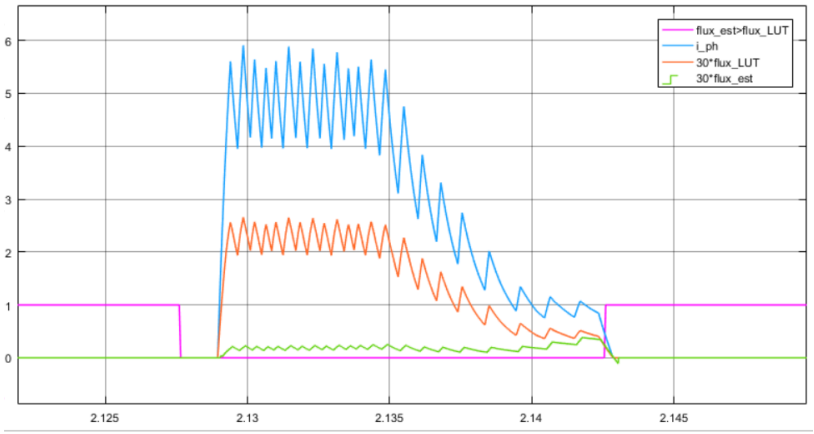


Figure 4.22: Flux linkage estimation. Flanks (purple) are obtained when estimated flux linkage (green) is larger than the reference flux linkage (orange).

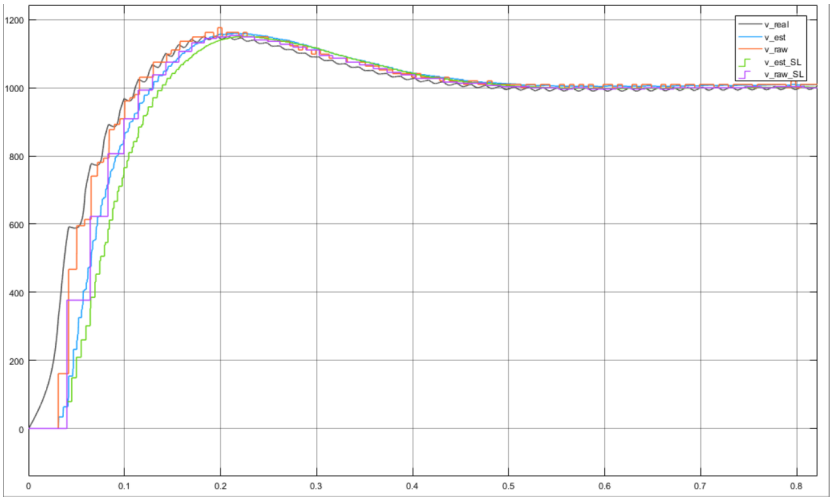


Figure 4.23: Sensorless speed estimation, raw (purple) and filtered (green) values compared with hall sensor speeds (blue and orange) and real speed (gray).

In figure 4.22, the flux linkage estimation method can be seen working in simulations. As can be seen in figure 4.24, the sensorless position estimation takes about 0.1 s before it starts estimating the position well. This is due to there being a large angle between the sensorless flanks (90° mech. instead of 30° mech. with the Hall sensor) and due to the machine accelerating (the position estimation model described in section 3.5.4 doesn't account for acceleration). At high, relatively constant speeds,

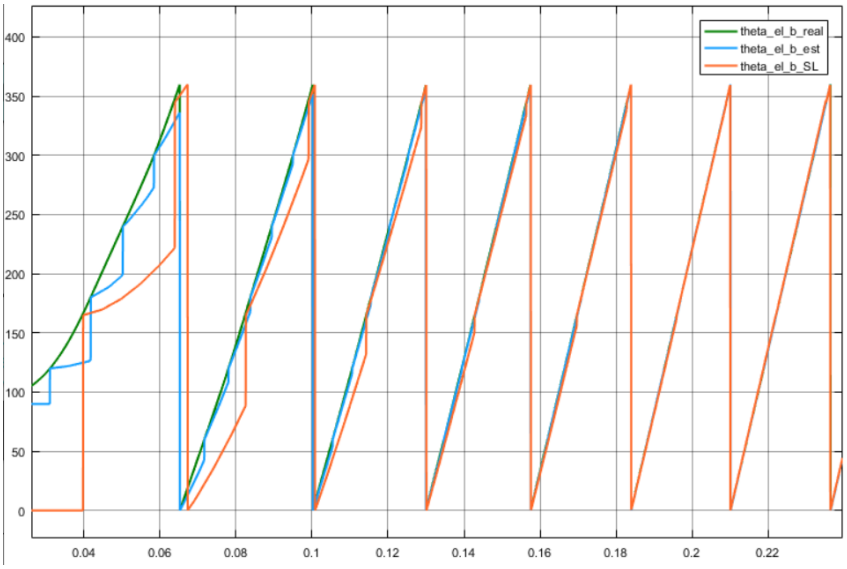


Figure 4.24: Sensorless position estimation (orange) based on filtered sensorless speed values, compared with hall sensor position (blue) and real position (green).

the method works fine, however.

Implementing the chosen sensorless control method with ATC instead of ITC would likely have been a better choice. ITC requires accurate position estimates at all times as its current reference is variable with position. The ATC is less reliant on the position since it only updates its current reference once every commutation period (four times per revolution).

The sensorless method implemented in this thesis is rudimentary and should if anything be seen as a proof of concept. It shows that magnetic characteristics of the SRM can be estimated in order to estimate the rotor's position. In a real application, however, a more elaborate method would need to be implemented.

## 4.7 Resistance estimation

In figure 4.25, the resistance estimation can be seen working in Simulink simulations. Here, an initial guess of the phase resistance is set to $R_0 = 1.5\Omega$, seen in green in the left picture. The flux estimation (in the right picture) gets better as the estimated resistance value approaches the real value. By the fourth flux estimation, the estimation error (in blue) is close to 0 and the flux linkage looks like expected (see figure 4.25b). As discussed in section 3.9, the resistance estimation method is especially useful when driving the SRM without a position sensor because the flux linkage estimation method improves. In fact, it is probably essential for it to work. When using the flux linkage estimation method, it is important to estimate the flux linkage well right from turn on of the machine.

Three things can be made to estimate the flux linkage correctly from the start:

1. Measure the phase resistance carefully to obtain a good guess of the initial resistance, $R_0$.
2. Measure the voltage over the phase and use that when integrating (in equation 2.16).
3. Estimate the resistance with the method described above.

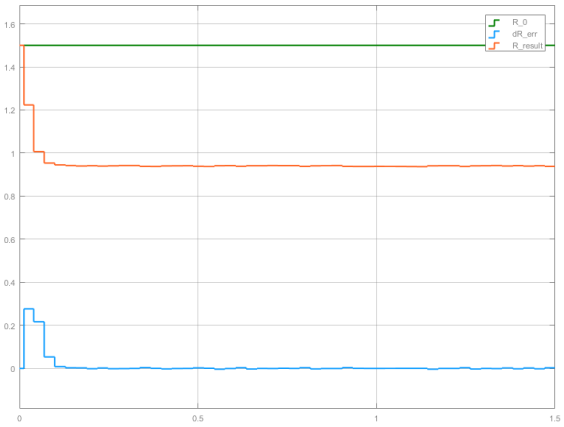


(a) The initial resistance value (green), the estimated resistance value (red) and the resistance error (blue).

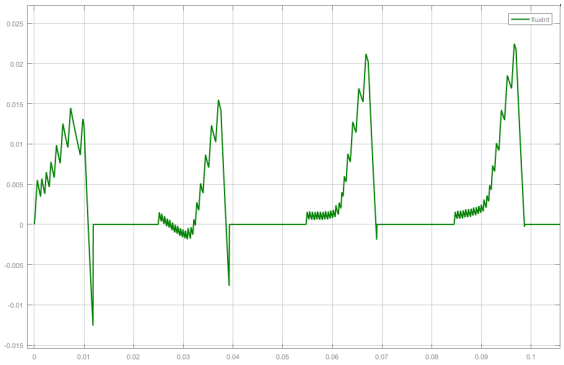

(b) The estimated flux linkage.

Figure 4.25: The resistance estimation algorithm in Simulink

# Chapter 5

# Conclusion

## 5.1 Methodology and performance of the control methods

Two ways of producing LUTs for an SRM controller, FEA simulations and experimental measurements, are investigated where both show promising results. The look-up tables generated by FEA simulation show some discrepancies to the measured ones. This could be explained by inaccurate geometrical measurements of the rotor and lack of material data of the machine. Even with these shortcomings, the simulations agree adequately with the real machine. Thus, it is deemed favorable to use FEA simulations as a tool to design the SRM controller in regard to time efficiency and practicality, without necessarily losing accuracy. The measured LUTs, however, are useful for verifying the FEA.

Both ITC and ATC are implemented and results show that the optimized ATC slightly outperforms the ITC. These results are unexpected since, in theory, ITC control should be able to outperform the ATC in regard to torque ripple and speed ripple. It is believed, however, that these results are a consequence of the 4/2 configuration of the machine and in other machines, where it is possible to generate a smooth torque, the ITC would be favorable. It is noteworthy to mention that if an optimized ATC should be implemented, an adequate simulation model with LUTs is still necessary. Therefore, while the ATC current reference profile is more primitive, it is not easier to implement in practice.

## 5.2 SRM for BorgWarner

Evaluating the competitiveness of the SRM in comparison to the existing BLDC solution is one of the purposes of the thesis. Following, some of the key points from the thesis are discussed in order to evaluate the prospects of using the SRM for BorgWarner.

When specifically looking at the asymmetric 4/2 SRM, it is obvious that it has some fundamental weaknesses. The first one is the inherent high torque ripple which leads to high speed ripple in the testing rig. The high torque ripple is not necessarily a deal breaker though. Mounting the SRM to a pump filled with oil might reduce

its speed ripple due to damping effects of the system. Further, the 4/2 is difficult to control sensorless due to the low number of phases. An advantage in sensorless control of the SRM is that phase resistance can easily be estimated on the fly since the phase current is 0 periodically. This is not the case in a BLDC where the currents are constantly changing during operation and more advanced estimation algorithms need to be implemented. In sensorless control of the 4/2 SRM, however, the disadvantages outweigh the advantages. Another benefit previously discussed is having a low number of phases from a cost perspective. At smaller sizes like in this application it reduces converter costs.

By including SRMs with other configurations in the analysis, the comparison becomes more interesting. Configurations with more stator and rotor poles are generally much more promising than the 4/2 SRM. Torque ripple can be reduced, thanks to the overlapping torque regions, with a combination of ITC control (or similar) and a well-designed torque share function. It is confirmed by modern literature and academic papers on the subject that it is possible to have competitive levels of torque ripple with an SRM. Another benefit of choosing an SRM with a higher pole number is that it enables multiple induction based sensorless methods, which are often effective at lower speeds. The possibility of running the machine sensorless is likely a necessity for BorgWarner since reducing costs is crucial in the competitive automotive industry.

The SRM's strengths lie in its cheap and robust design. However, at the current price, the permanent magnet cost is quite a small part of the whole actuator cost in BorgWarner's case, according to people in the company. Depending on the future price of permanent magnets, BorgWarner might be more or less interested in the SRM. SRM converters today are slightly more expensive and less available than the BLDC versions. But the reason is because they are less demanded, and not because they use more expensive components. An asymmetric bridge converter can be built using the same amount and types of components as a BLDC converter. Another possibility is using common H-bridges, as done in this thesis. It is not as efficient use of components, but a possibility for prototyping. A cost comparison was set as part of the thesis goal but was never thoroughly investigated. The thesis instead focused on performance and implementation, but if the SRM should be fairly evaluated a cost analysis should be performed.

We believe that the next step for BorgWarner, in evaluating the competitiveness of the SRM, is to examine an SRM with a higher amount of stator and rotor poles. All in all, the SRM is an interesting machine as an alternative to the BLDC and could theoretically perform at similar levels while securing the company against future costs due to resource scarcity.

# Bibliography


[1] Berker Bilgin, James Weisheng Jiang, and Ali Emadi. *Switched Reluctance Motor Drives, Fundamentals to Applications*. Taylor & Francis Group, LLC, 2019.

[2] Karen Smith Stegen. "Heavy rare earths, permanent magnets, and renewable energies: An imminent crisis". In: *Energy Policy (ELSEVIER)* (Apr. 2015).

[3] Thomas Finken, Mathias Felden, and Kay Hameyer. "Comparison and design of different electrical machine types regarding their applicability in hybrid electrical vehicles". In: *Proceedings of the 2008 International Conference on Electrical Machines (IEEE)* (Oct. 2008).

[4] Nobukazu Hoshi Masatsugu Takemoto Akira Chiba Kyohei Kiyota and Satoshi Ogasawara. "Development of a Rare-Earh-Free SR Motor With High Torque Density for Hybrid Vehicles". In: *IEEE Transactions on Energy Conversion, VOL 30* (Mar. 2015).

[5] Shih-Chieh Gu Ray-LE Lin Hsiao-Ping Chi. "High Electromechanical-Effciency Resonant Miller-type Driver for Switched Reluctance Motors". In: *International Conference on Power Electronics and Drive Systems (PEDS)* (Nov. 2009).

[6] T.J.E. Miller. *Electronic Control of Switched Reluctance Machines*. Elsevier, 2001.

[7] Piotr Bogusz et al. "A Two-phase Switched Reluctance Motor with Asymmetrical Rotor for a High-speed Drive". In: *International Conference on Electrical Drives and Power Electronics (EDPE)* (Sept. 2015).

[8] Antti Lehikoinen. *How to perform electromagnetic FEA*. Accessed: 2020-12-18. Oct. 2019. URL: `https://enterfea.com/electromagnetic-fea/`.

[9] Lars Sjöberg. "Torque Control of a Novel Switched Reluctance Machine". PhD thesis. Lunds Tekniska Högskola (LTH), 1996.

[10] Mats Alaküla, Per Karlsson, and Hans Bängtsson. *Power Electronics*. Lund University, 2019.

[11] T.J.E. Miller et al. "Instantaneous Torque Control of Electric Motor Drives". In: *TRANSACTIONS ON POWER ELECTRONICS (IEEE)* (Jan. 1987).

[12] He Cheng, Hao Chen, and Chou Yang. "Average Torque Control of Switched Reluctance Machine Drives for Electrical Vehicles". In: *IET Electric Power Applications (IET)* (Aug. 2015).

[13] Hala Hannoun, Mickaël Hilairet, and Claude Marchand. "Design of an SRM Speed Control Strategy for a Wide Range of Operating Speeds". In: *IEEE Transactions on Industrial Electronics (IEEE)* (Sept. 2010).

[14] Mahmoud Hamouda and László Számel. "Reduced Torque Ripple based on a Simplified Structure Average Torque Control of Switched Reluctance Motor for Electric Vehicles". In: *IEEE International Conference and Workshop in Óbuda on Electrical and Power Engineering (IEEE)* (Oct. 2018).

[15] Marcelo Vinícius de Paula, Tárcio André dos Santos Barros, and Pedro José Dos Santos Neto. *A Review of Classic Torque Control Techniques for Switched Reluctance Motors*. InTechOpen, 2020.

[16] Christos Mademlis and Iordanis Kioskeridis. "Performance Optimization in Switched Reluctance Motor Drives With Online Commutation Angle Control". In: *IEEE TRANSACTIONS ON ENERGY CONVERSION (IEEE)* (Sept. 2003).

[17] Jae-Hoon Kim and Rae-Young Kim. "Sensorless Direct Torque Control Using the Inductance Inflection Point for a Switched Reluctance Motor". In: *IEEE Transactions on Industrial Electronics (IEEE)* (2018).

[18] J. P. Lyons, S. R. MacMinn, and M. A. Preston. "Flux/current methods for SRM rotor position estimation". In: *Conference Record of the IEEE Industry Applications Society Annual Meeting (IEEE)* (Sept. 1991).

[19] R Hrbac et al. "Estimation of On-Fly Phase Resistance of on 8/6 Switched Reluctance Motor for Sensorless Control". In: *Elektronika Ir Elektrotechnika* (May 2014).

[20] Radim Visinka. "3-Phase Switched Reluctance (SR) Sensorless Motor Control Using a 56F80x, 56F8100 or 56F8300 Device". In: *NXP* (Feb. 2005).

[21] Mohamed Rashed et al. "Sensorless Indirect-Rotor-Field-Orientation Speed Control of a Permanent-Magnet Synchronous Motor With Stator-Resistance Estimation". In: *IEEE TRANSACTIONS ON INDUSTRIAL ELECTRONICS (IEEE)* (June 2007).

[22] S. Sangwongwanich T. Furuhashi and S. Okuma. "A position and velocity sensorless control for brushless DC motors using an adaptive sliding mode observer". In: *" IEEE Trans. Ind. Electron (IEEE)* (Apr. 1992).

[23] Babak Nahid-Mobarakeh, Farid Meibody-Tabar, and François-Michel Sargos. "Mechanical Sensorless Control of PMSM With Online Estimation of Stator Resistance". In: *IEEE TRANSACTIONS ON INDUSTRY APPLICATIONS (IEEE)* (Mar. 2004).